Electronic Supplementary Material (ESI) for Chemical Science.
This journal is © The Royal Society of Chemistry 2018

Supporting Information for

Electrophile-Promoted Fe-to-N_2 Hydride Migration in Highly Reduced Fe(N_2)(H) Complexes

Meaghan M. Deegan and Jonas C. Peters

Division of Chemistry and Chemical Engineering
California Institute of Technology
Pasadena, CA 91125 United States

Table of Contents

Experimental Details

1.1 General Considerations

All manipulations were carried out using standard Schlenk or glovebox techniques under an N_2 atmosphere. Solvents were deoxygenated and dried by thoroughly sparging with N_2 followed by passage through an activated alumina column in a solvent purification system by SG Water, USA LLC. Ethereal solvents (THF, Et_2O, DME) were dried further by stirring over Na/K alloy (>2 h) and were filtered through Celite prior to use. Deuterated benzene was purchased from Cambridge Isotope Laboratories, Inc., and dried by refluxing over Ca-H then distilled and stored over Na. Deuterated THF was purchased from Cambridge Isotope Laboratories and dried over Na/K alloy and was filtered through Celite prior to use. Reagents were purchased from commercial vendors and used without further purification unless otherwise noted. $P_3^BFe(N_2)$ **3** and $P_3^B(\mu\text{-H})Fe(H)(N_2)$ **1** were prepared according to literature procedures.[1,2,3]

1.2 Physical Methods

NMR spectra (^1H, ^{13}C, ^{31}P, ^{11}B, and ^{29}Si) were collected at room temperature (25 °C unless specified) on Varian 300, 400, or 500 MHz spectrometers. ^1H, ^{13}C, and ^{29}Si chemical shifts are reported in ppm, relative to tetramethylsilane using residual proton and ^{13}C resonances from solvent as internal standards. ^{29}Si NMR chemical shifts were determined from ^{29}Si-HMBC two-dimensional spectra. ^{31}P chemical shifts are reported in ppm relative to 85% aqueous H_3PO_4 and ^{11}B spectra were referenced to $BF_3 \bullet Et_2O$. Thin film IR spectra were obtained using a Bruker Alpha Platinum ATR spectrometer with OPUS software in a glovebox under an N_2 atmosphere. UV-Vis measurements were collected using a Cary 50 instrument with Cary WinUV software. X-band EPR spectra were obtained on a Bruker EMX spectrometer on solutions prepared as frozen glasses in 2-MeTHF. Mössbauer spectra were recorded on a spectrometer from SEE Co. (Edina, MN) operating in the constant acceleration mode in a transmission geometry. The sample was kept in an SVT-400 cryostat from Janis (Wilmington, MA). The quoted isomer shifts are relative to the centroid of the spectrum of a metallic foil of α-Fe at room temperature. Solution samples were prepared by freezing solutions in a Delrin cup in a glovebox with rapid transfer of frozen samples to a liquid nitrogen bath before mounting in the cryostat. Samples were collected with no applied magnetic field unless otherwise specified. Data analysis was performed using the program WMOSS (www.wmoss.org) and quadrupole doublets were fit to Lorentzian lineshapes.

X-Ray diffraction and combustion analysis measurements were carried out in the Beckman Institute Crystallography Facility. XRD measurements were collected using a dual source Bruker D8 Venture, four-circle diffractometer with a PHOTON CMOS detector or a Brüker Apex II diffractometer with an APEX II CCD detector. Structures were solved using SHELXT and refined against F^2 on all data by full-matrix least squares with SHELXL. The crystals were mounted on a glass fiber under Paratone N oil. See below for any special refinement details for individual data sets. Combustion analysis measurements were collected using a PerkinElmer 2400 Series II CHN Elemental Analyzer by facility staff.

(1) H. Fong, M.-E. Moret, and J. C. Peters, *Organometallics,* 2013, **32**, 3053.
(2) T. J. Del Castillo, N. B. Thompson, and J. C. Peters, *J. Am. Chem. Soc.*, 2016, **138**, 5341.
(3) M.-E. Moret, and J. C. Peters, *Angew. Chem. Int. Ed.*, 2011, **50**, 2063.

2. Synthetic Details

$[P_3^B(\mu\text{-}H)Fe(H)(N_2)][K_2(THF)_n]$ 2: A yellow-orange THF solution (~20 mM) of $P_3^B(\mu\text{-}H)Fe(H)(N_2)$ **1** was cooled to -78 °C. To this solution, an excess of KC_8 was added with the mixture turning very dark brown/black upon the addition of reductant. After stirring for 3 min at -78 °C, the suspension was filtered through a prechilled Celite pipette filter to remove excess KC_8 and graphite. Characterization of this complex and studies of its reactivity were done using material that was generated *in situ* according to this procedure because of the extreme air and moisture sensitivity of this complex as well as its apparent thermal instability (solutions of the complex were observed to completely decompose over the course of hours at room temperature in a sealed J. Young NMR tube under a nominally inert atmosphere). To generate X-Ray quality crystals of this complex, the THF was removed *in vacuo* and the residue was redissolved in a 2:1 mixture of dimethoxyethane and toluene and layered with pentane at -35 °C. $^{31}P\{^1H\}$ NMR (THF-d_8; 162 MHz): δ 92.6 (d, J = 59 Hz, 2P) -1.5 (s, 1P). ^1H NMR (THF/THF-d_8; 400 MHz): δ 7.67 (Ar C-*H*, br, 1H), 7.53 (Ar C-*H*, d, J = 6.5 Hz, 2H), 7.26 (Ar C-*H*, 1H), 7.02 (Ar C-*H*, d, J = 6.3 Hz, 2H), 6.88 (Ar C-*H*, m, 2H), 6.57 (Ar C-*H*, m, 4H), 2.21 (PC-*H*, overlapping, br, 6H), 1.15 (CH_3, m, 12H), 0.91 (CH_3, dd, J = 11, 7 Hz, 6H), 0.79 (CH_3, q, J = 6 Hz, 6H), 0.70 (CH_3, dd, J = 12, 7 Hz, 6H), 0.61 (CH_3, q, J = 6 Hz, 6H), -18.19 (Fe-*H*-B, br, 1H), -20.78 (Fe-H, td, J = 64.8, 8.5 Hz, 1H). $^{11}B\{^1H\}$ NMR (THF/THF-d_8; 128 MHz): δ 1.72 (br). IR of $[P_3^B(\mu\text{-}H)Fe(H)(N_2)][K_2(THF)_n]$ (thin film, cm^{-1}) : ν_{NN} = 1746 cm^{-1}. Mössbauer (80 K; frozen THF solution, mm/s): δ = 0.25; ΔE_Q = 2.28. The extreme sensitivity and thermal instability of this complex precluded obtaining satisfactory EA of this complex

$[P_3^BFe(H)(N_2)][K(benzo\text{-}15\text{-}crown\text{-}5)_2]$ 4: A stirring THF solution of $P_3^BFe(N_2)$ **3** (293 mg, 0.434 mmol) was cooled to -78 °C. To this solution, a slight excess of $KHBEt_3$ (1.0 M in THF, 520 μL, 0.521 mmol, 1.2 equiv) was added and the mixture was stirred at -78 °C for 3 h and then warmed to room temperature and stirred for an additional 30 min. A THF solution of benzo-15-crown-5 (0.955 mmol, 2.2 equiv) was added and the mixture was stirred for an additional 15 min. The solvent was removed *in vacuo* and the resulting orange solid was redissolved in a minimal amount of THF and layered with pentane at -35 °C overnight. The mother liquor was decanted and the material was washed with additional pentane (5 mL), yielding the product as an orange, crystalline solid (472 mg, 87%). Crystalline material suitable for XRD analysis was prepared similarly. $^{31}P\{^1H\}$ NMR (THF-d_8; 162 MHz): δ 77.1. $^{31}P\{^1H\}$ NMR (THF-d_8; 202 MHz, -80 °C): δ 95.5 (d, 1P), 79.3 (s, 1P), 59.7 (d, 1P). ^1H NMR (THF-d_8; 400 MHz): δ 7.10 (Ar C-*H*, br, 3H), 7.05 (Ar C-*H*, br, 3H), 6.62 (Ar C-*H*, br, 3H), 6.50 (Ar C-*H*, br, 3H), 2.31 (PC-*H*, br, 6H), 1.08 (CH_3, br, 18H), 0.87 (CH_3, br, 18H), -12.59 (Fe-H, q, J = 46 Hz, 1H). $^{11}B\{^1H\}$ NMR (THF-d_8; 128 MHz): δ 5.8. IR of $[P_3^BFe(H)(N_2)][K(benzo\text{-}15\text{-}crown\text{-}5)_2]$ (thin film, cm^{-1}) : ν_{N2} = 1956 cm^{-1};($\nu_{Fe\text{-}H}$ overlaps with the intense N_2 stretch). Mössbauer (80 K; frozen THF solution, mm/s): δ = 0.20; ΔE_Q = 0.84. Attempts to obtain satisfactory EA invariably gave slightly low values for N, which may be due to some lability. Anal. Calcd. for $C_{64}H_{95}BFeKN_2O_{10}P_3$: C 61.44; H 7.65; N 2.24. Found: C 61.28; H 8.03; N 1.66.

$[P_3^B(\mu\text{-}H)Fe(H)(NNSi^iPr_3)][K(THF)]$ 5: A THF solution of $[P_3^B(\mu\text{-}H)Fe(H)(N_2)][K_2(THF)_n]$ **2** was generated from **1** (103.8 mg, 0.153 mmol) *in situ* at -78 °C. A prechilled Et_2O solution of the silylating reagent $^iPr_3SiCl$ (26.6 mg, 0.138 mmol, 0.9 equiv) was added and the mixture was stirred at -78 °C for 15 min then warmed to room temperature and stirred for an additional 15 min. The solvent was removed *in vacuo* from the resultant brown solution, the residue was

triturated with pentane and then extracted into pentane. The solvent was again removed and the brown residue was redissolved in benzene and lyophilized, yielding the product as a brown powder (101.9; 78% yield). Single crystals suitable for X-ray diffraction were grown by dissolving this powder in a 1:1 Et_2O/pentane mixture and allowing the solvent to evaporate slowly in a vessel containing MeCy at -35 °C. $^{31}P\{^1H\}$ NMR (C_6D_6; 162 MHz): δ 90.6 (br, 2P), -1.0 (1P). ^1H NMR (C_6D_6; 400 MHz): δ 7.91 (Ar C-*H*, br s, 1H), 7.86 (Ar C-*H*, d, *J* = 7.5 Hz, 2H), 7.51 (Ar C-*H*, d, *J* = 7.5 Hz, 1H), 7.2-7.1 (Ar C-*H*, multiple resonances overlapping C_6H_6, 4H), 6.99 (Ar C-*H*, t, *J* = 7.5 Hz, 2H), 6.91 (Ar C-*H*, t, *J* = 7 Hz, 2H), 2.40 (^{i}Pr C-*H*, m, 2H), 1.95 (^{i}Pr C-*H*, m 2H), 1.87 (^{i}Pr C-*H*, br, 2H), 1.42 (^{i}Pr-C*H*$_3$, dd, *J* = 12, 6.5 Hz, 6H), 1.23 (^{i}Pr-C*H*$_3$, s, 18H), 1.25-1.1 (^{i}Pr-C*H*$_3$, overlapping m, 21H) 1.03 (^{i}Pr-C*H*, s, 3H), 0.97 (^{i}Pr-C*H*$_3$, q, *J* = 7 Hz, 9H), -9.71 (Fe-*H*, t, *J* = 84 Hz, 1H), -11.08 (B-*H*-Fe, br s, 1H). $^{11}B\{^1H\}$ NMR (C_6D_6; 128 MHz): δ 2.1 (br). ^{29}Si NMR (C_6D_6; 79 MHz): δ -5.6. IR of [P_3^B(μ-H)Fe(H)(NSi^{i}Pr$_3$)][K(THF)] (thin film, cm^{-1}) : ν_{NN} = 1537, 1577; $\nu_{Fe\text{-}H}$ = 1757, 1816; $\nu_{B\text{-}H\text{-}Fe}$ = 2078 (br). Anal. Calcd. for $C_{49}H_{84}BFeKN_2OP_3Si$: C 62.35; H 8.97; N 2.97. Found: C 61.92; H 9.10; N 2.77.

P_3^B(μ-H)Fe(H)(NNSi$_2$) 7: A THF solution of [P_3^B(μ-H)Fe(H)(N_2)][K_2(THF)$_n$] was generated *in situ* at -78 °C. A prechilled Et_2O solution of the disilylating reagent Si_2Cl_2 (Si_2 = $Me_2Si(CH_2CH_2)SiMe_2$; 0.9 equiv) was added to a stirred solution of the dianionic Fe complex and stirred at -78 °C for five minutes changing from dark brown to green in color, indicating conversion to the disilylhydrazido(2-) complex **7**. This species could be generated *in situ* and characterized in solution at low temperature. Attempts to crystallographically characterize this species in the solid state were unsuccessful, likely due its high solubility in nonpolar solvents and thermal instability. Variable temperature NMR spectra for this complex are shown below. ^{31}P NMR (THF/THF-d_8; 202.4 MHz; -40 °C): δ 100.5 (br, 2P), -8.0 (s, 1P). ^1H NMR (THF/THF-d_8; 500 MHz; -40 °C): 7.43 (Ar C*H*, br, 2H), 7.34 (Ar C*H*, d, *J* = 7 Hz, 1H), 6.96 (Ar C*H*, t, *J* = 7 Hz, 1H), 6.89 (Ar C*H*, t, *J* = 7, 2H), 6.82 (Ar C*H*, t, *J* = 7.5, 2H), 6.78 (Ar C*H*, t, *J* = 7.5, 1H), 6.66 (Ar *CH*, d, *J* = 7.5 Hz, 2H), 6.29 (Ar C*H*, d, *J* = 7 Hz, 1H), 2.86 (^{i}Pr C*H*, br, 4H), 2.46 (^{i}Pr C*H*, br, 2H), 1.48 (^{i}Pr-C*H*$_3$, dd, *J* = 13.5, 7 Hz, 6H), 1.34 (^{i}Pr-C*H*$_3$, br, 6H), 1.17 (^{i}Pr-C*H*$_3$, br, 6H), 0.98 (^{i}Pr-C*H*$_3$, dd, *J* = 11, 7 Hz, 6H), 0.69 (^{t}Pr-C*H*$_3$, br, 9H), 0.67 (Si-C*H*$_2$, s, 4H), 0.38 (Si-C*H*$_3$, s, 6H), 0.21 (Si-C*H*$_3$, s, 6H), -16.58 (B-*H*-Fe, br, 1H), -17.32 (Fe-*H*, t, *J* = 91 Hz, 1H). Three of the phosphine isopropyl methyl resonances are not accounted for in this assignment; these may be located under the solvent resonances. UV-vis (THF, nm {M^{-1} cm^{-1}}, -80 °C): 660 {240}.

P_3^B(μ-H)Fe(NHNSi$_2$)(CN^{t}Bu) 9: A THF solution of [P_3^B(μ-H)Fe(H)(N_2)][K_2(THF)$_n$] was generated *in situ* from **1** (88.2 mg, .130 mmol) at -78 °C. A prechilled Et_2O solution of the disilylating reagent Si_2Cl_2 (Si_2 = $Me_2Si(CH_2CH_2)SiMe_2$; 25.3 mg, .117 mmol, 0.9 equiv) was added to a stirred solution of the dianionic Fe complex and stirred at -78 °C for five minutes. Neat ^{t}BuNC (5 equiv, 74 μL, 0.652 mmol) was added via syringe and the mixture was allowed to warm to room temperature and was stirred for an additional hour. The solvent was removed *in vacuo*, and the deep red residue was extracted into pentane and filtered through Celite. The solvent was again removed and the residue was redissolved in a minimum of pentane and crystallized overnight via solvent evaporation in a vessel containing methylcyclohexane. X-Ray quality crystals were prepared according to this procedure. To complete purification, the crystalline material was cooled to -78 °C and washed with prechilled pentane. After warming to room temperature, the crystals were extracted into benzene and lyophilized, yielding the product

as a fine red powder (79.7 mg; 75%). $^{31}P\{^{1}H\}$ NMR (C_6D_6; 162 MHz): δ 88.9 (d, J = 19 Hz, 1P), 82.7 (d, J = 19 Hz, 1P), -2.1 (s, 1P). ^{1}H NMR (C_6D_6; 400 MHz): δ 7.84 (N*H*, s, 1H), 7.73 (Ar C*H*, br, 1H), 7.55 (Ar C*H*, t, J = 8.5 Hz, 2H), 7.44 (Ar C*H*, dt, J = 6, 3 Hz, 1H), 7.38 (Ar C*H*, t, J = 7 Hz, 1H), 7.21 (Ar C*H*, m, overlapping benzene, 1H), 7.13 (Ar C*H*, m, overlapping benzene, 3H), 7.02 (Ar C*H*, t, J = 7 Hz, 1H), 6.95 (Ar C*H*, br, 2H), 2.77 (^{i}Pr C*H*, sept, J = 7.5 Hz, 2H), 2.50 (^{i}Pr C*H*, m, 1H), 2.19 (^{i}Pr C*H*, br, 2H), 1.99 (^{i}Pr C*H*, sept, J = 7.5 Hz, 1H), 1.55 (^{i}Pr C*H*$_3$, dd, J = 13, 7 Hz, 3H), 1.60-0.90 (^{i}Pr C*H*$_3$, overlapping m, 36H), 1.31 (CN^{t}Bu, s, overlapping, 9H), 0.68 (Si C*H*$_2$, d, J = 3.5 Hz, 4H), 0.34 (Si C*H*$_3$, s, 6H), -0.08 (C*H*$_3$, s, 6H), -10.42 (B-H-Fe, br, 1H). $^{11}B\{^{1}H\}$ NMR (C_6D_6; 128 MHz): δ 7.9. IR of P_3^B(μ-H)Fe(NHN(Si_2))(CN^{t}Bu) (thin film, cm^{-1}): ν_{CN} = 1997; $\nu_{N\text{-}H}$ = 3197; $\nu_{B\text{-}H\text{-}Fe}$ = 2090 (br). IR of P_3^B(μ-D)Fe(NDN(Si_2))(CN^{t}Bu) (thin film, cm^{-1}): $\nu_{N\text{-}D}$ = 2377; $\nu_{B\text{-}D\text{-}Fe}$ = 1510 (br). Anal. Calcd. for $C_{47}H_{81}BFeN_3P_3Si_2$: C 62.45; H 9.03; N 4.65. Found: C 63.06; H 9.44; N 4.22.

[(P_3^B-H)Fe(CN^{t}Bu)][B($C_8H_3F_6$)$_4$]: A solution of P_3^B(μ-H)Fe(NHNSi_2)(CN^{t}Bu) **9** (28.5 mg, 0.0315 mmol, 1 equiv) in Et_2O (2 mL) was cooled to -78 °C. To this solution, a prechilled solution of [H(OEt_2)$_2$][B($C_8H_3F_6$)$_4$] (28.7 mg, 0.0284 mmol, 0.9 equiv) in Et_2O (2 mL) was added. The mixture was allowed to stir at -78 °C for 30 min then warmed to room temperature and stirred for an additional 30 min. The solvent was removed *in vacuo*, and the remaining purple foam was washed with pentane and then extracted into Et_2O. Isolation of the product as a crystalline purple solid was carried out by layering a concentrated Et_2O solution with pentane at -35 °C (35.1 mg, 77%). Crystals suitable for XRD analysis could be obtained in this fashion. ^{19}F NMR (THF-d_8; 376 MHz): δ -61.5. ^{1}H NMR (THF-d_8; 400 MHz): δ 28.7 (br), 11.7, 9.8, 7.8, 7.5, 5.3, 5.0, -0.5, -6.3. IR spectrum (thin film, cm^{-1}): $\nu_{B\text{-}H}$ = 2483; ν_{CN} = 2115.

Quantification of NH_2NSi_2: A solution of P_3^B(μ-H)Fe(NHNSi_2)(CN^{t}Bu) **9** (25.3 mg, 0.028 mmol, 1 equiv) was dissolved in Et_2O (2 mL) and cooled to -78 °C. Similarly a solution of [H(OEt_2)$_2$][B($C_8H_3F_6$)$_4$] (28.3 mg, 0.028 mmol, 1 equiv) in Et_2O (2 mL) was cooled to -78 °C. The acid solution was added to the solution of **9** and the mixture was allowed to stir at low temperature for 10 min then at room temperature for an additional 30 min. After stirring was complete, the solutions were exposed to air and an aqueous solution of HCl was added (2 mL, 1 M in THF). After 24 h of stirring at room temperature, hydrazine could be detected according to the standard colorimetric method[4] using a reported calibration curve[5] (Yields of four runs: 57%, 61%, 62%, 66%). No NH_3 was detected in these reaction mixtures using the indophenol method.[6]

(4) G. W. Watt, and J. D. Crisp, *Anal. Chem.*, 1952, **24**, 2006.
(5) J. Fajardo Jr., and J. C. Peters, *J. Am. Chem. Soc.*, 2017, **139**, 16105.
(6) M. W. Weatherburn, *Anal. Chem.*, 1967, **39**, 971.

3. NMR Spectra

$[P_3^B(\mu\text{-}H)Fe(H)(N_2)][K_2(THF)_n]$ 2.

Figure S1. ^{1}H NMR spectrum (400 MHz) of **2** in THF/THF-d_8.

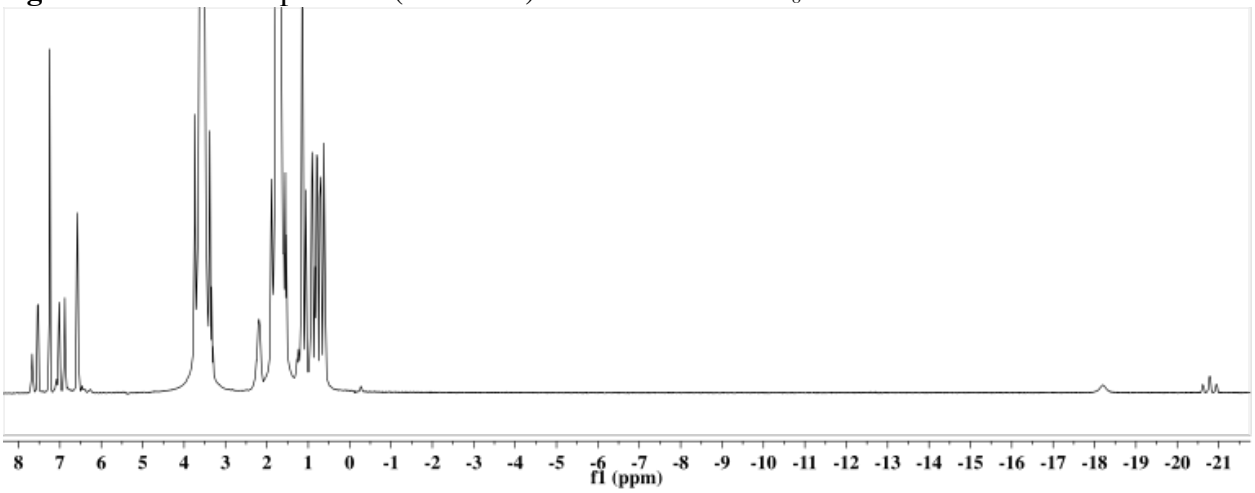

Figure S2. ^{31}P NMR spectrum (162 MHz) of **2** in THF/THF-d_8.

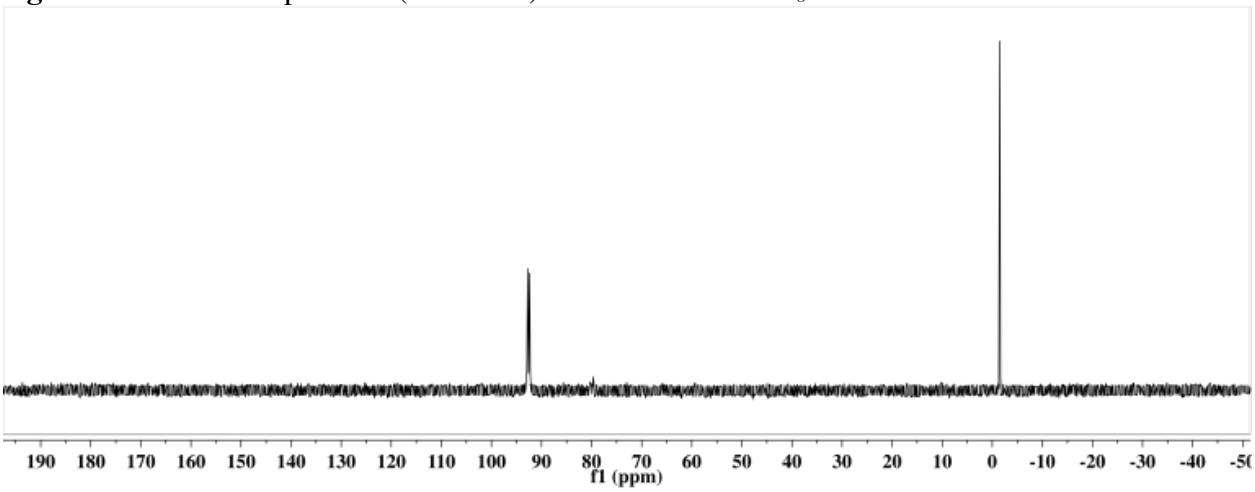

Figure S3. ^{11}B NMR spectrum (128 MHz) of **2** in THF/THF-d_8.

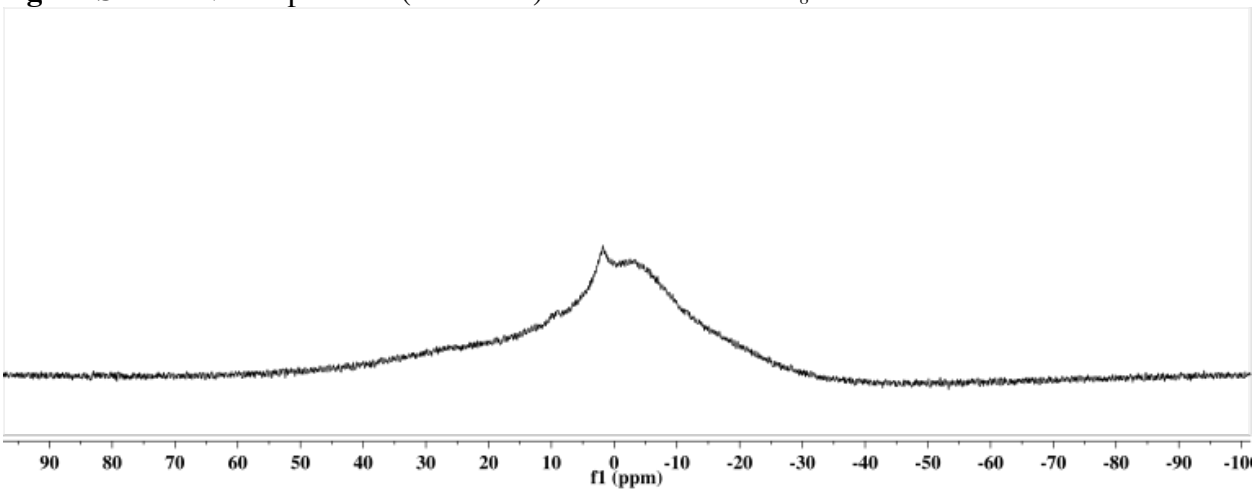

$[P_3^BFe(H)(N_2)][K(benzo\text{-}15\text{-}crown\text{-}5)_2]$ 4.

Figure S4. ^{1}H NMR spectrum (400 MHz) of **4** in THF-d_8.

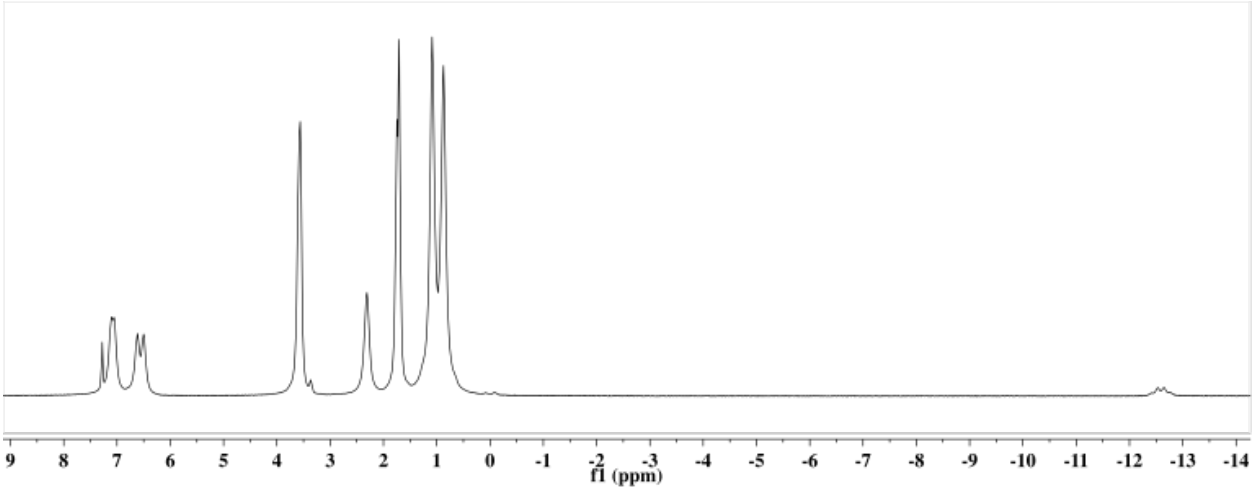

Figure S5. ^{31}P NMR spectrum (162 MHz) of **4** in THF-d_8.

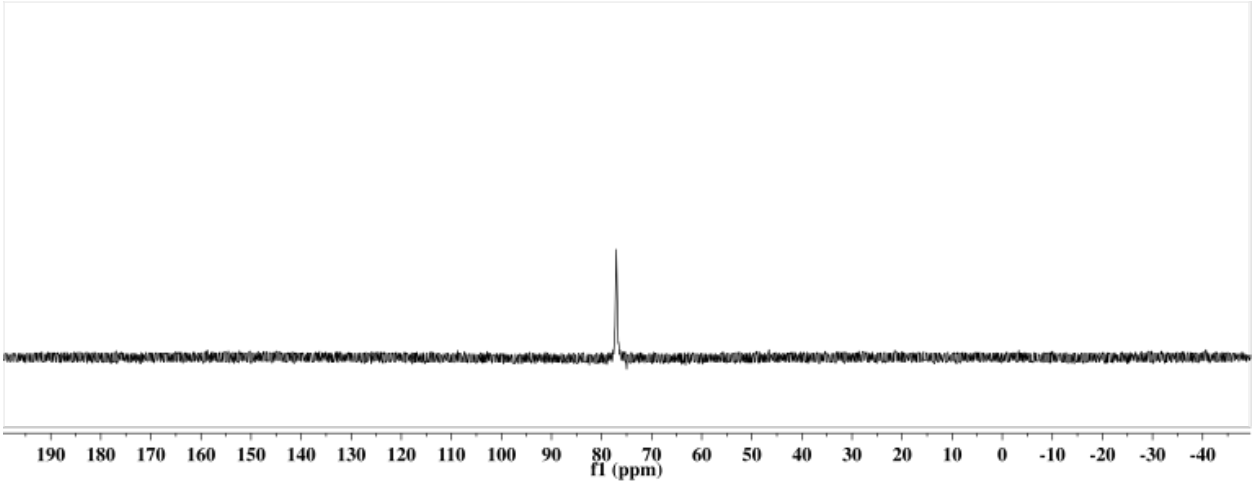

Figure S6. ^{31}P NMR spectrum (202 MHz) of **4** in THF-d_8 collected at -80 °C.

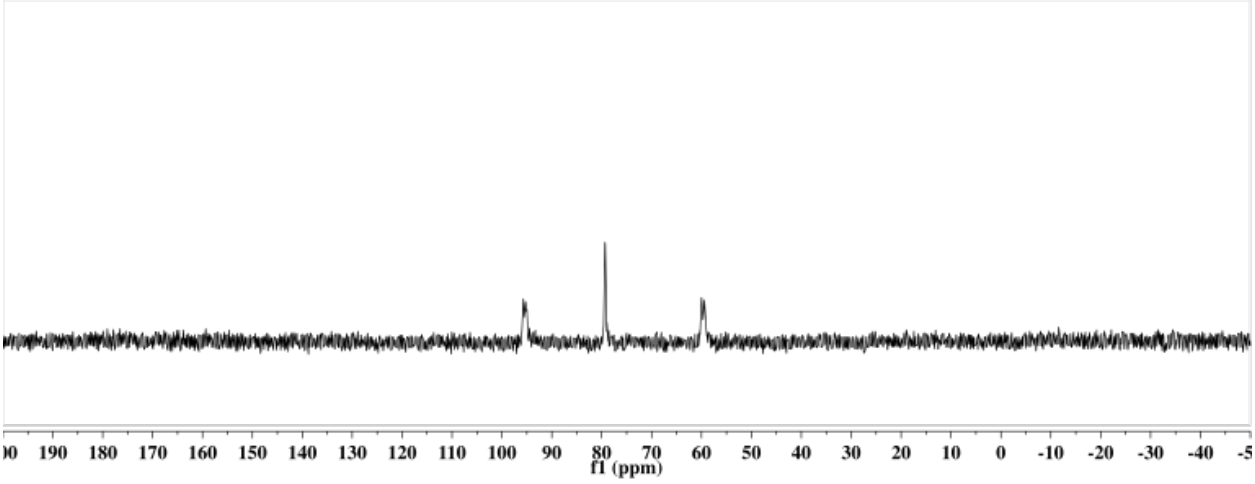

Figure S7. ^{11}B NMR spectrum (128 MHz) of **4** in THF-d_8.

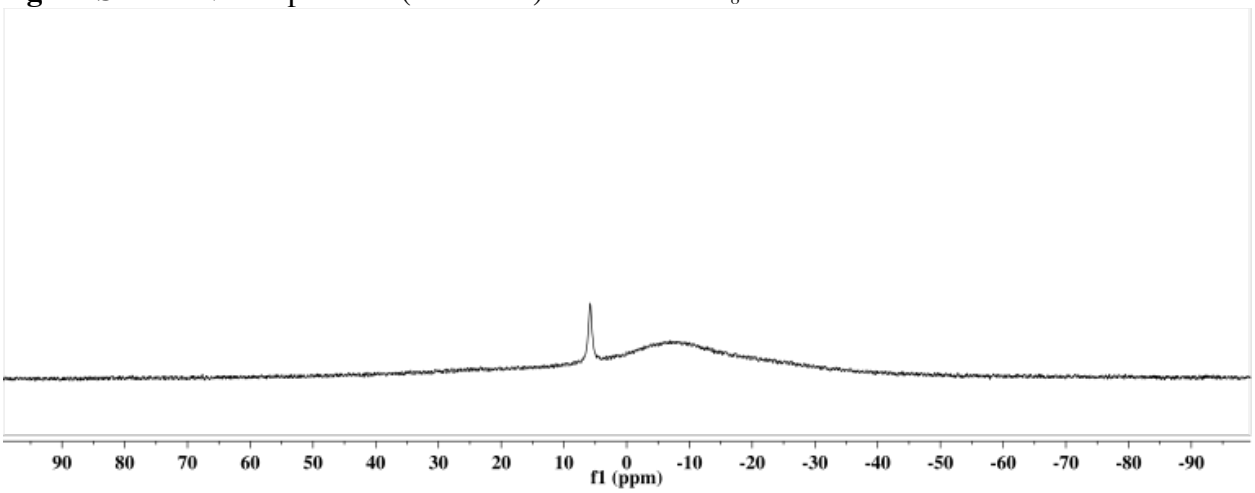

[P_3^B(μ-H)Fe(H)(NNSi^{i}Pr$_3$)][K(THF)] 5.

Figure S8. ^{1}H NMR (400 MHz) spectrum of **5** in C_6D_6.

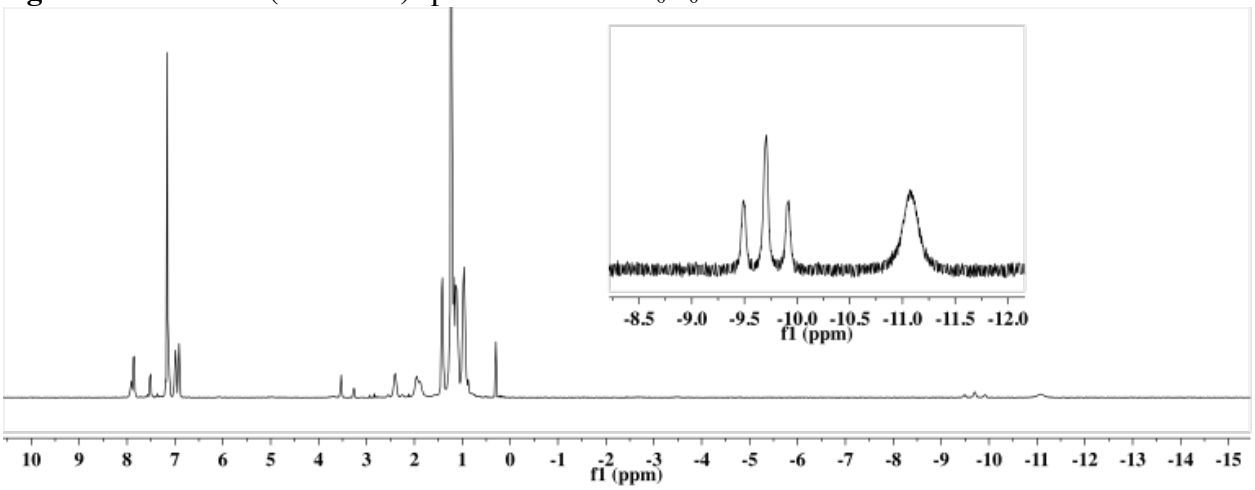

Figure S9. ^{31}P NMR spectrum (162 MHz) of **5** in C_6D_6.

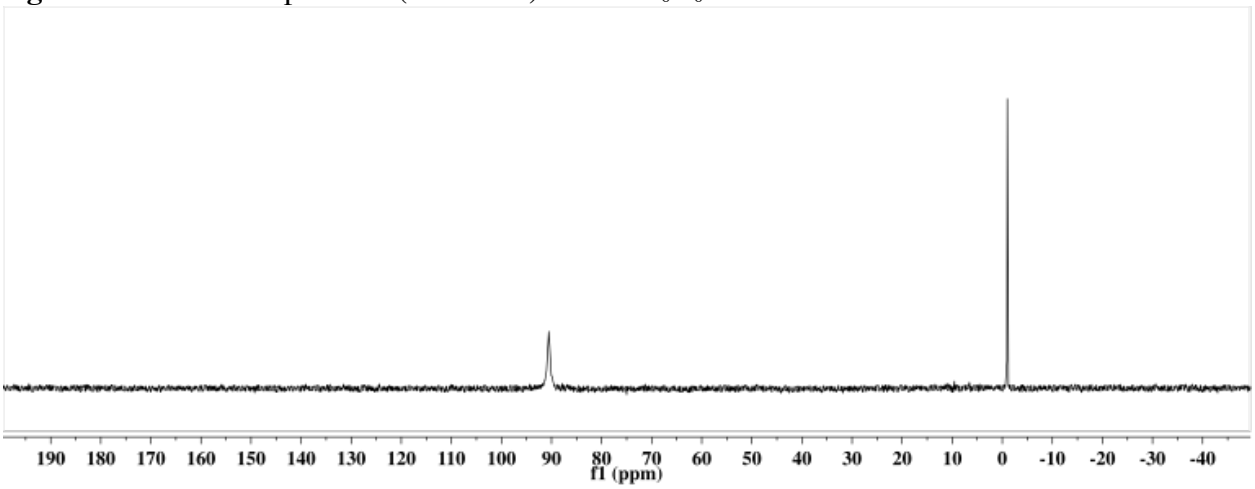

Figure S10. ^{11}B NMR spectrum (128 MHz) of **5** in C_6D_6.

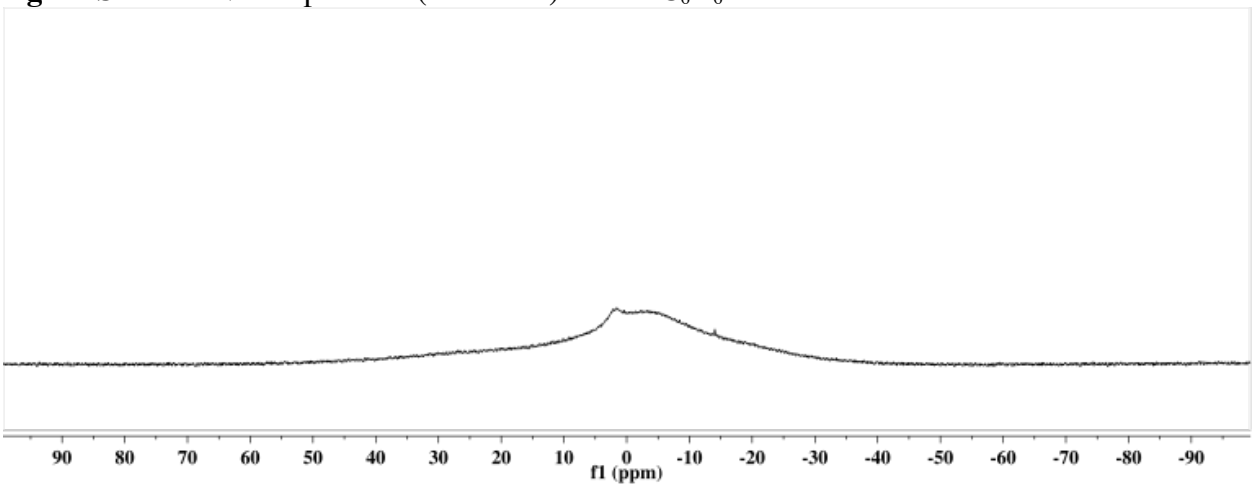

Figure S11. ^{29}Si-HMBC spectrum of **5** in C_6D_6.

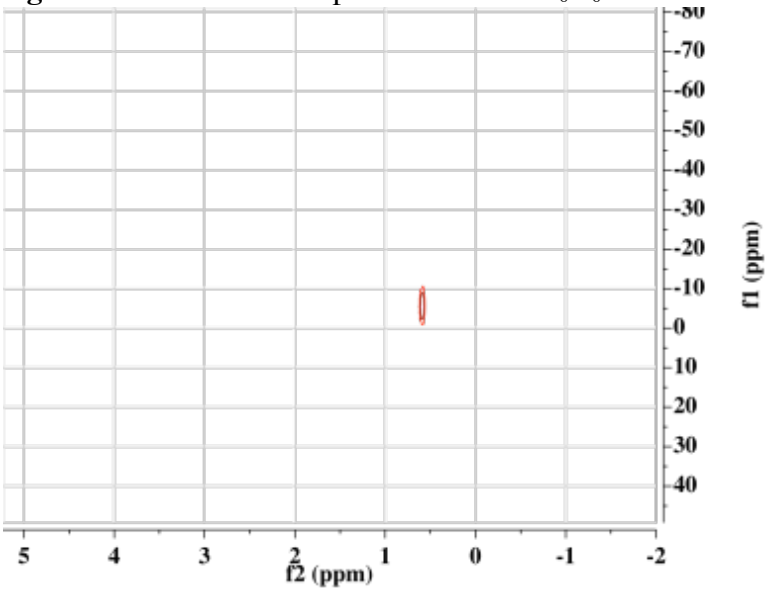

$P_3^B(\mu\text{-H})Fe(H)(NNSi_2)$ 7.

Figure S12. Variable temperature ^{1}H NMR data (500 MHz; THF/THF-d_8) for **7** collected in 10 degree increments starting at -80 °C (top), increasing to 10 °C (bottom). The paramagnetic product of N-H bond formation is observed in the spectra collected at 0 and 10 °C, with two of the resonances indicated by the # symbol.

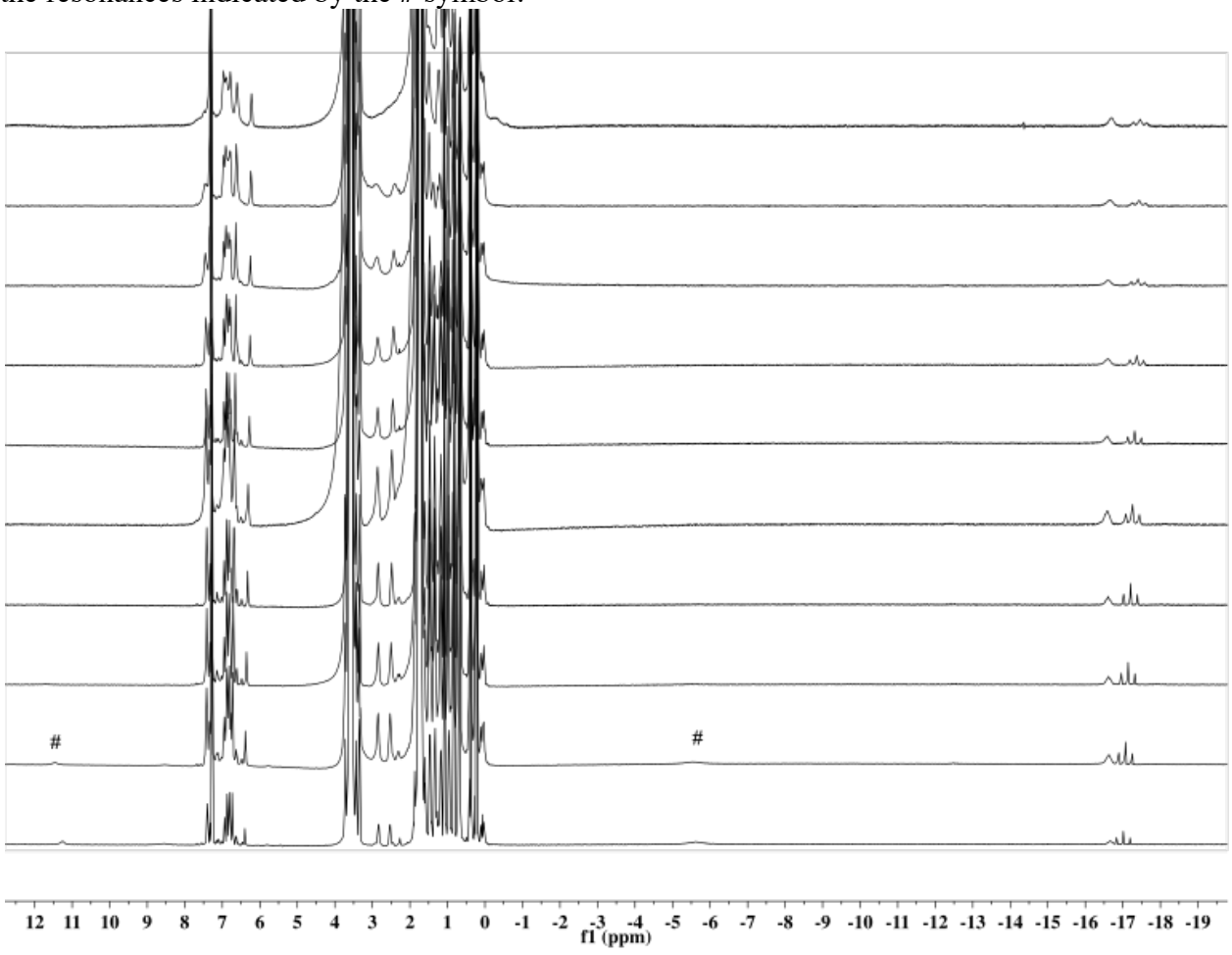

Figure S13. Variable temperature ^{31}P NMR (202.4 MHz; THF/THF-d_8) data for **7** collected in 10 degree increments starting at -80 °C (top), increasing to 10 °C (bottom).

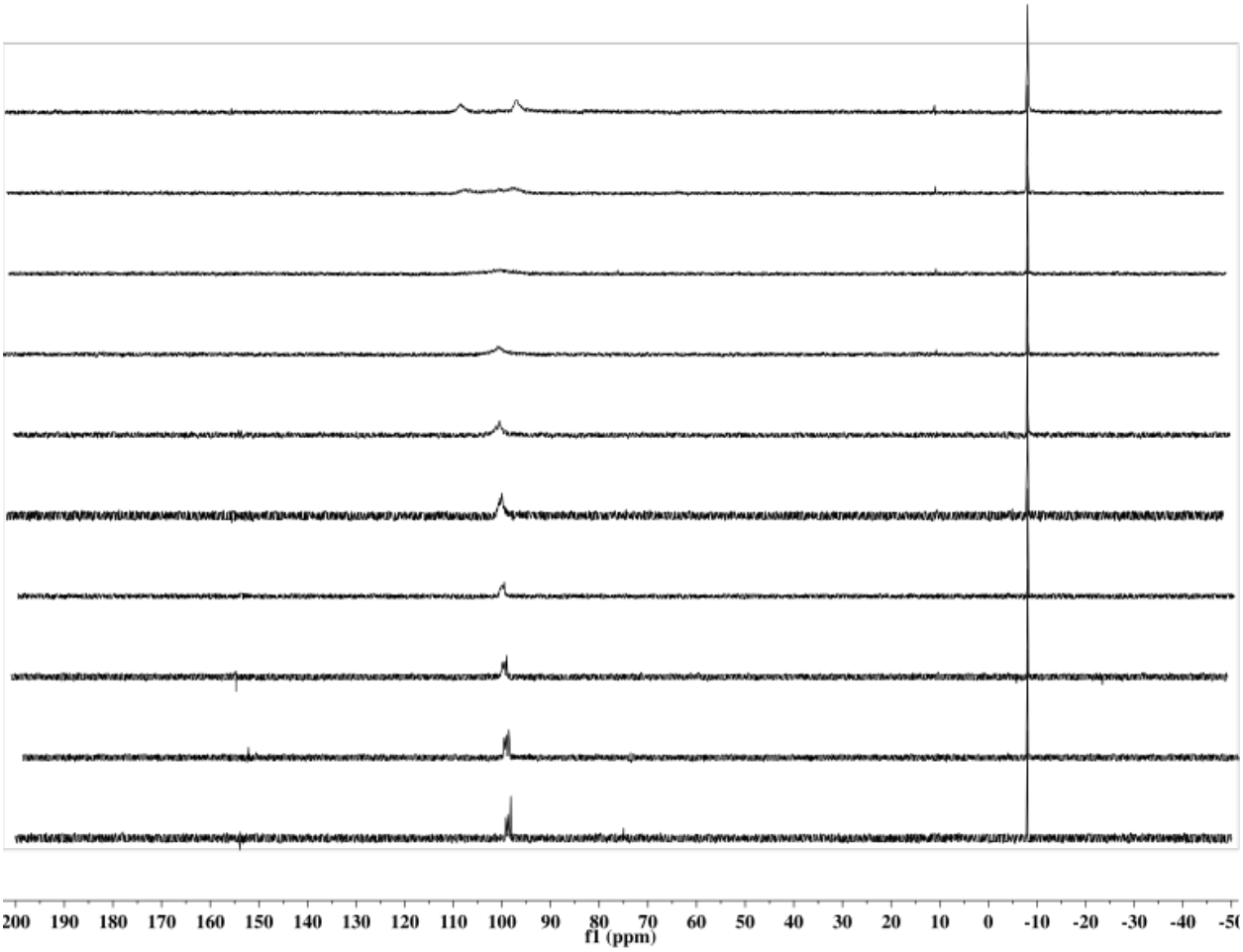

Figure S14. ^{1}H NMR spectrum (500 MHz) of **7** collected in THF/THF-d_8 at -40 °C.

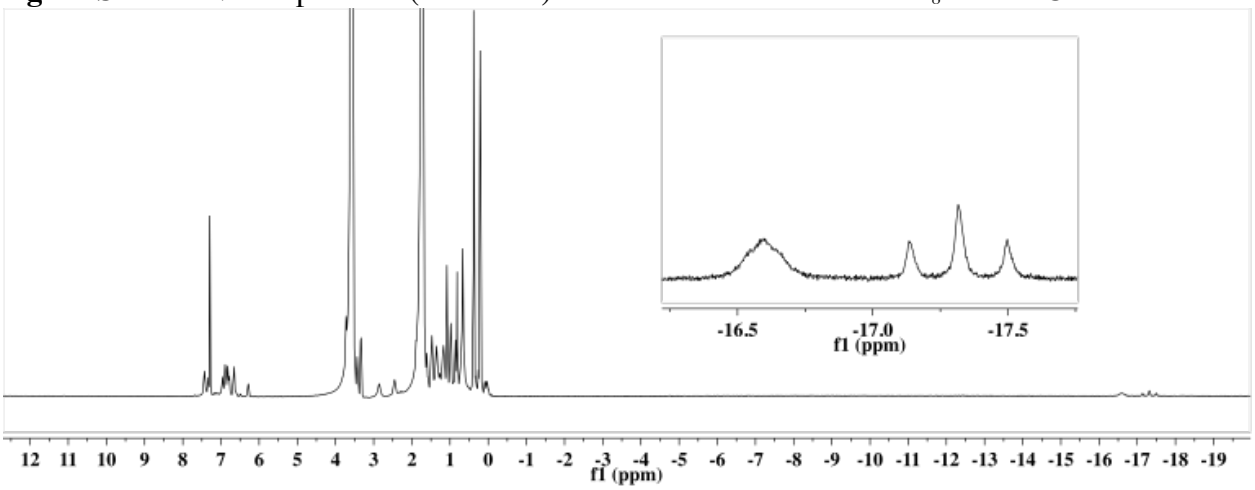

Figure S15. ^{31}P NMR spectrum (202 MHz) of **7** collected in THF/THF-d_8 at -40 °C.

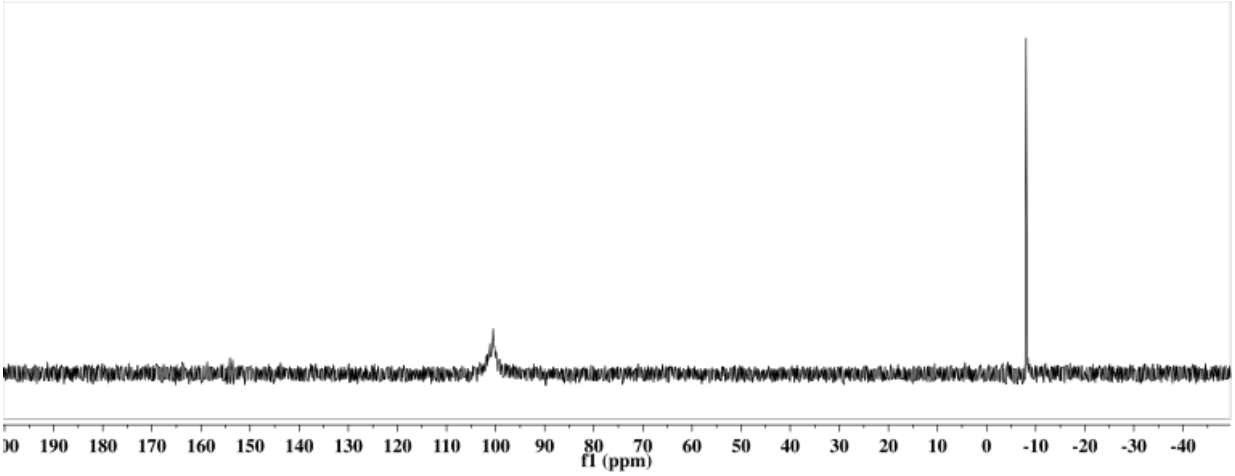

Observation of Decay of 7 to $P_3^B(\mu\text{-H})Fe(NHNSi_2)$ 8.

Figure S16. ^{1}H NMR spectrum (500 MHz) of a mixture containing **7** and **8** collected in THF/THF-d_8 at -10 °C.

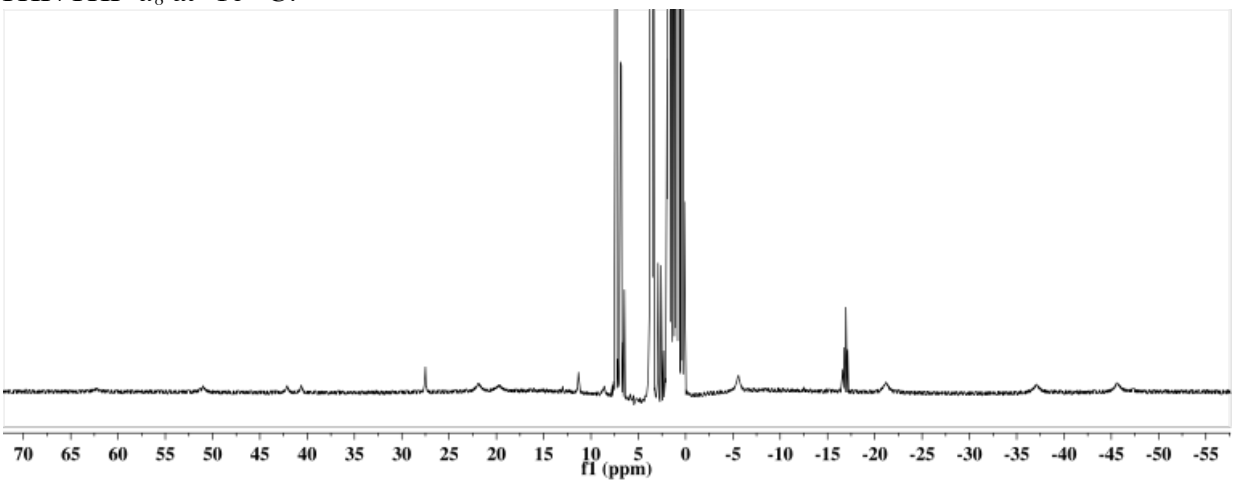

Figure S17. ^{1}H NMR spectrum (400 MHz; C_6D_6) containing predominantly **8** collected at RT. Minor peaks associated with the precursor **7** as well as the initial product of thermal decomposition are also apparent.

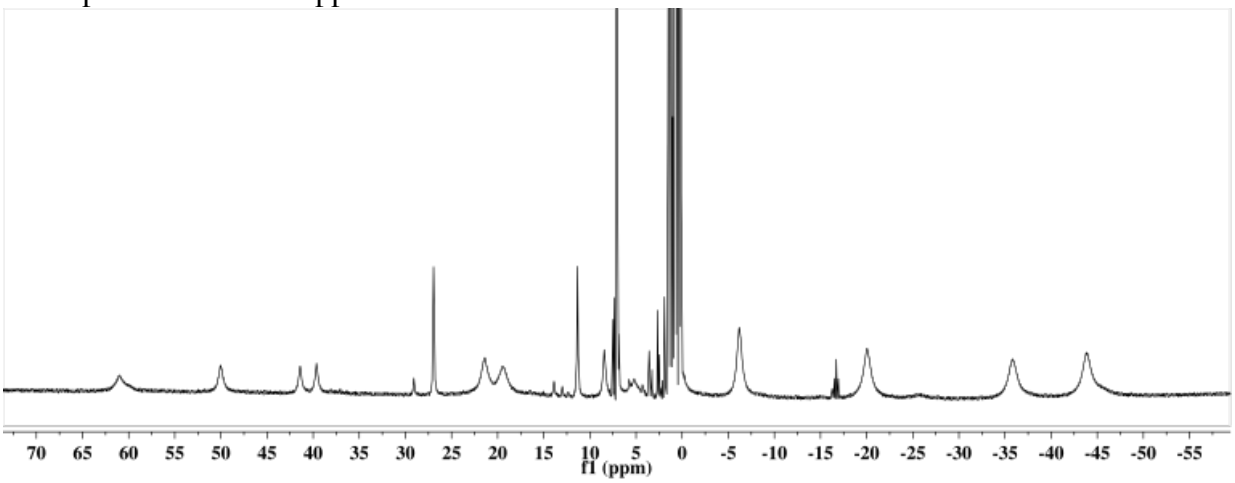

Figure S18. ^{1}H NMR spectrum (300 MHz; C_6D_6) showing complete consumption of **7** and the further decay of complex **8** to its initial decomposition product.

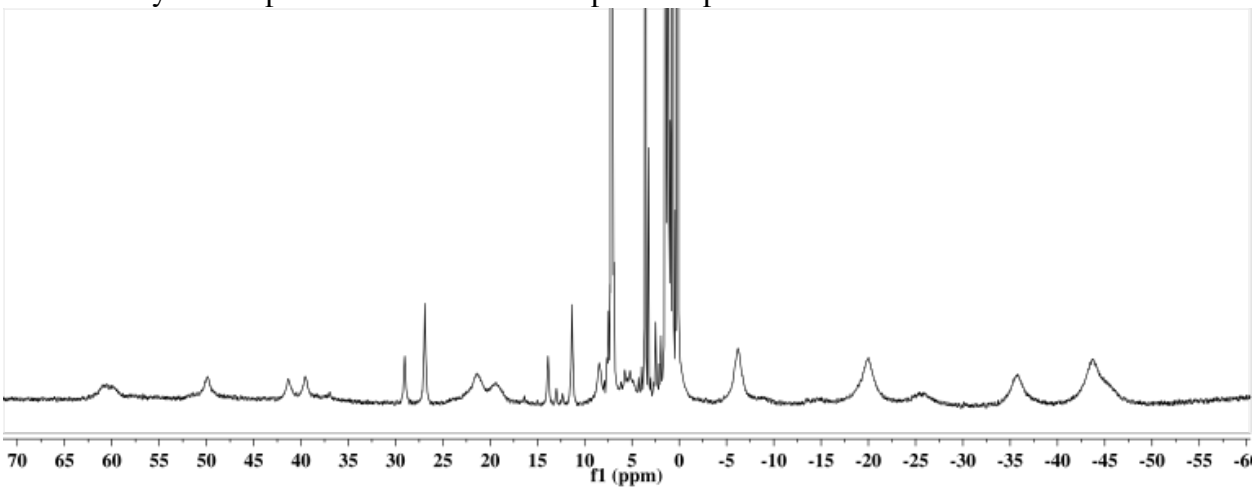

$P_3^B(\mu$-H)Fe(NHNSi$_2$)(CN^{t}Bu) 9.

Figure S19. ^{1}H NMR spectrum (400 MHz) of **9** in C_6D_6.

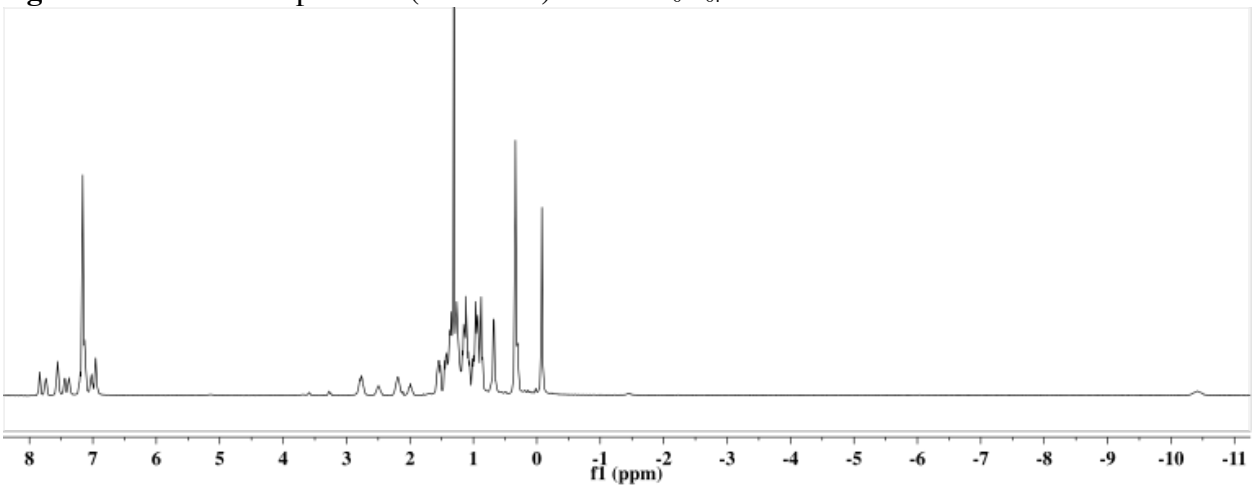

Figure S20. ^{1}H NMR spectrum (300 MHz) of **9-D$_2$** in C_6D_6 exhibiting the absence of the N-H and B-H-Fe resonances.

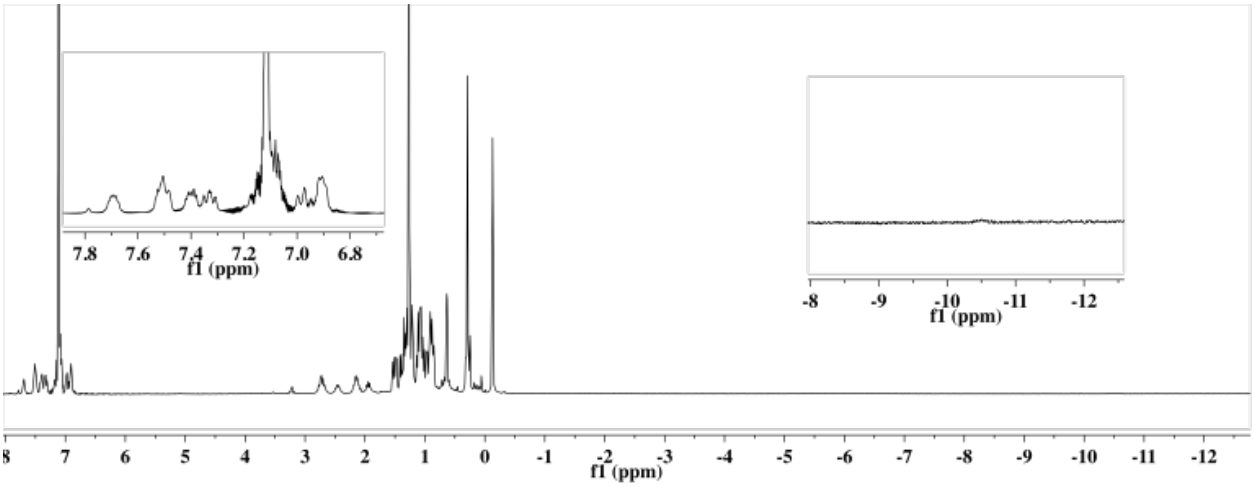

Figure S21. ^{31}P NMR spectrum (162 MHz) of **9** in C_6D_6.

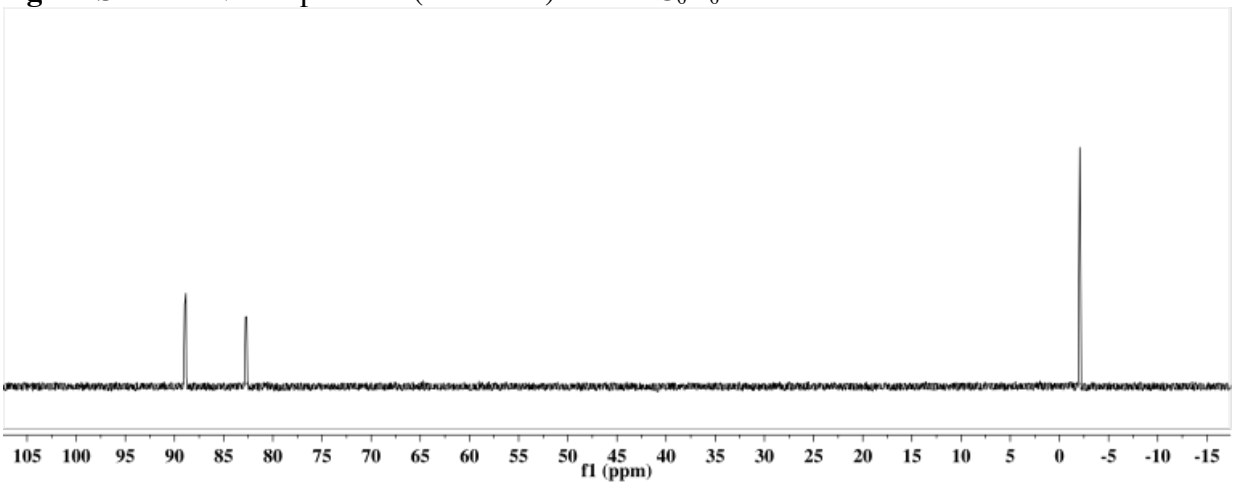

Figure S22. ^{11}B NMR spectrum (128 MHz) of **9** in C_6D_6.

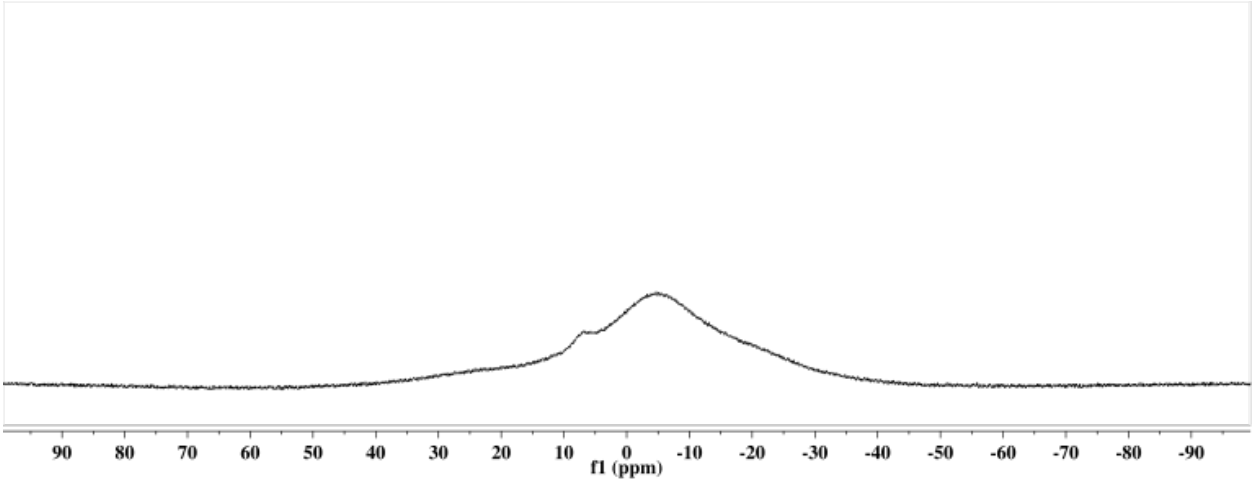

Figure S23. ^{29}Si-HMBC spectrum of **9** in C_6D_6. Weak coupling is observed to the α-N-H proton (7.84 ppm).

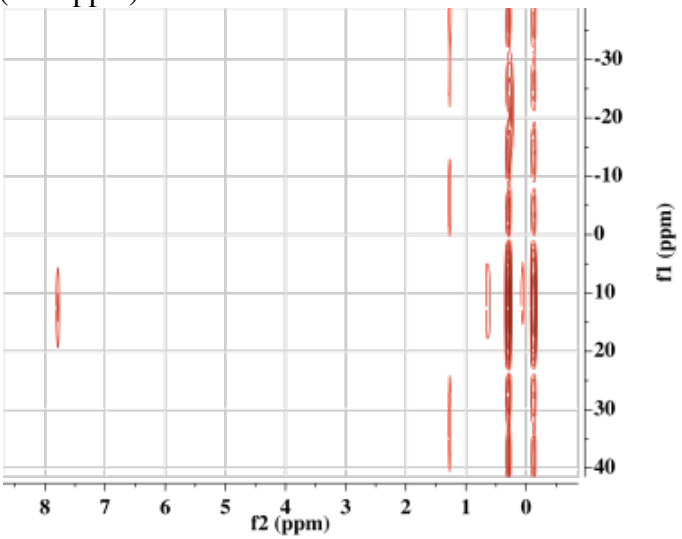

[(P_3^B-H)Fe(CN^{t}Bu)][B($C_8H_3F_6$)$_4$].

Figure S24. ^{1}H NMR spectrum (400 MHz) in THF-d_8.

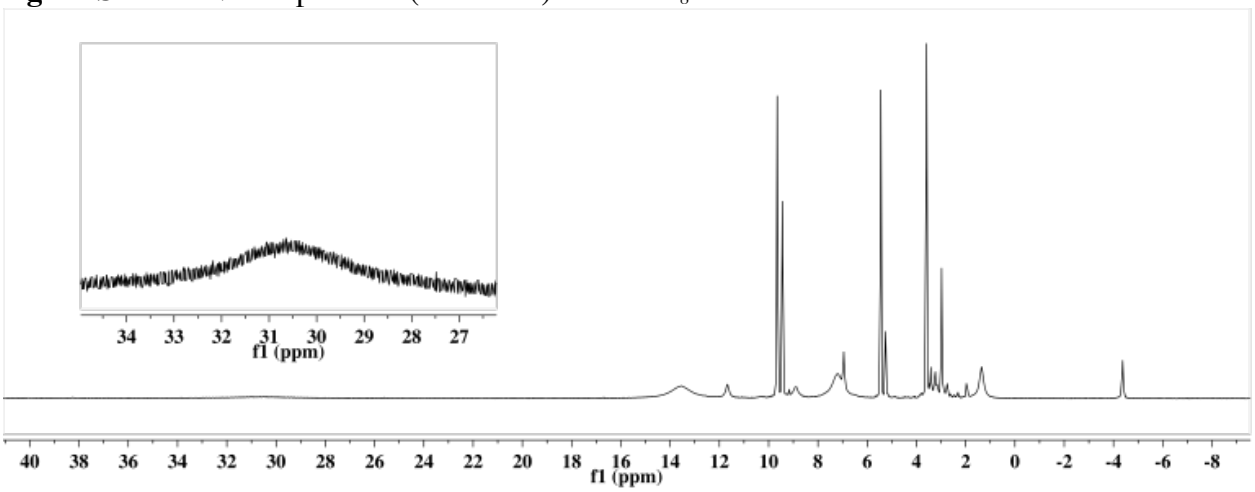

Figure S25. ^{19}F NMR spectrum (376 MHz) in THF-d_8.

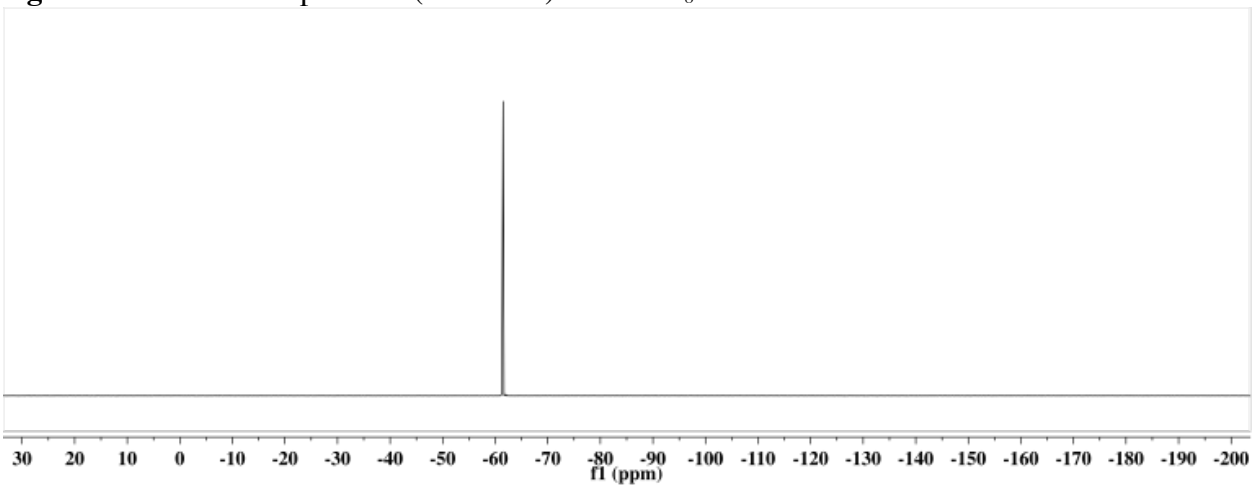

4. IR Spectra

Figure S26. IR spectrum of $[P_3^B(\mu\text{-H})Fe(H)(N_2)][K_2(THF)_n]$ **2** (thin film from THF).

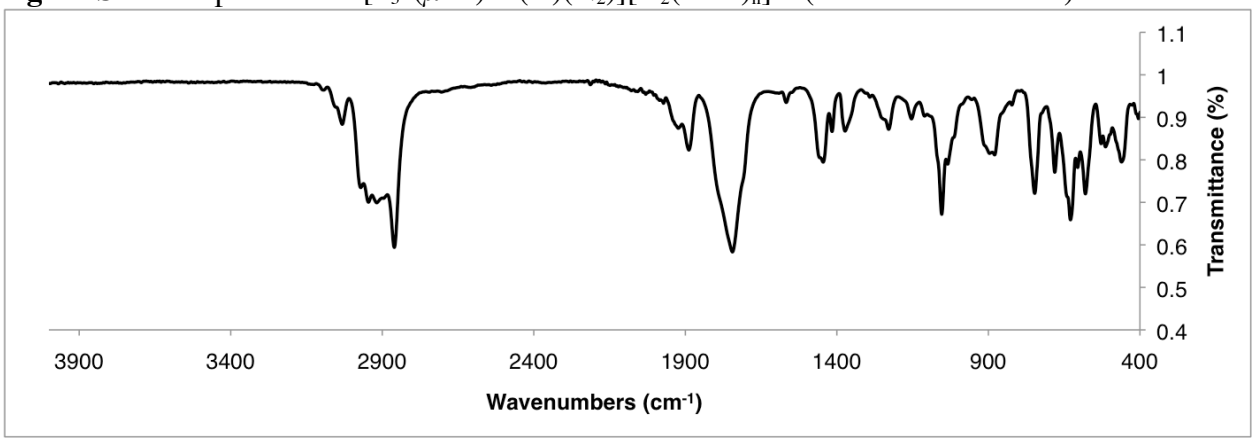

Figure S27. IR spectrum of $[P_3^BFe(H)(N_2)][K(benzo\text{-}15\text{-}crown\text{-}5)_2]$ **4** (solid state).

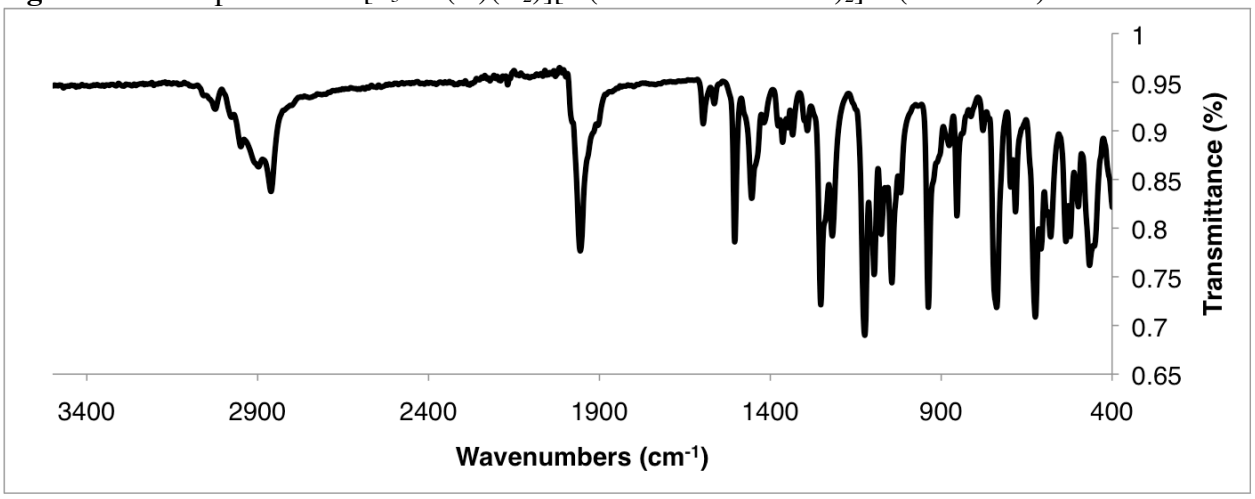

Figure S28. IR spectrum of $P_3^B(\mu\text{-H})Fe(H)(NNSi^iPr_3)$ **5**.

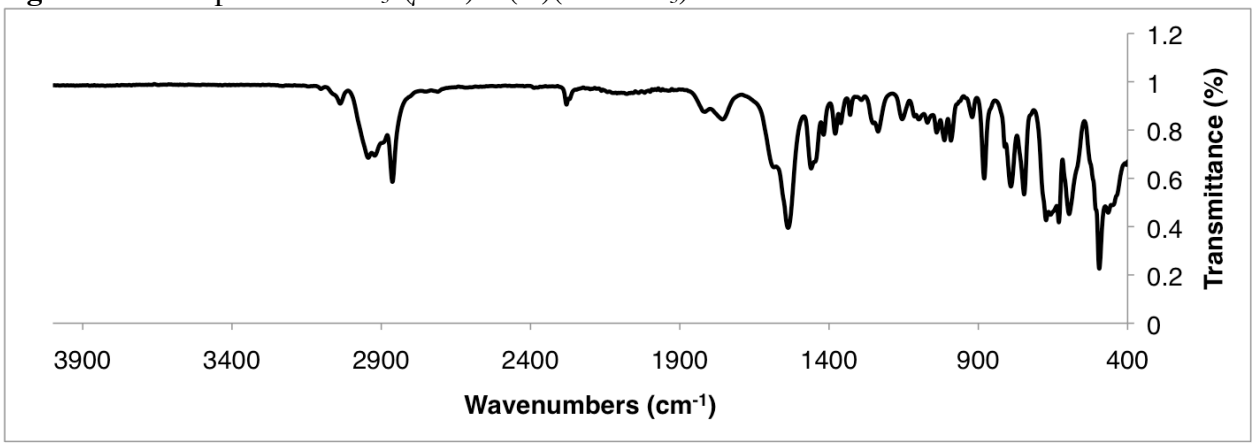

Figure S29. IR spectrum of $P_3^B(\mu\text{-H})Fe(NHNSi_2)$ **8** (thin film). The proposed N-H stretch is observed at 3263 cm^{-1} and is absent in the spectrum of **8-D_2** (Figure S4.5, below). Similarly, the B-H-Fe stretch is found at 1971 cm^{-1}. The presence of a minor N_2 containing impurity from an oxidation side reaction is indicated by #.

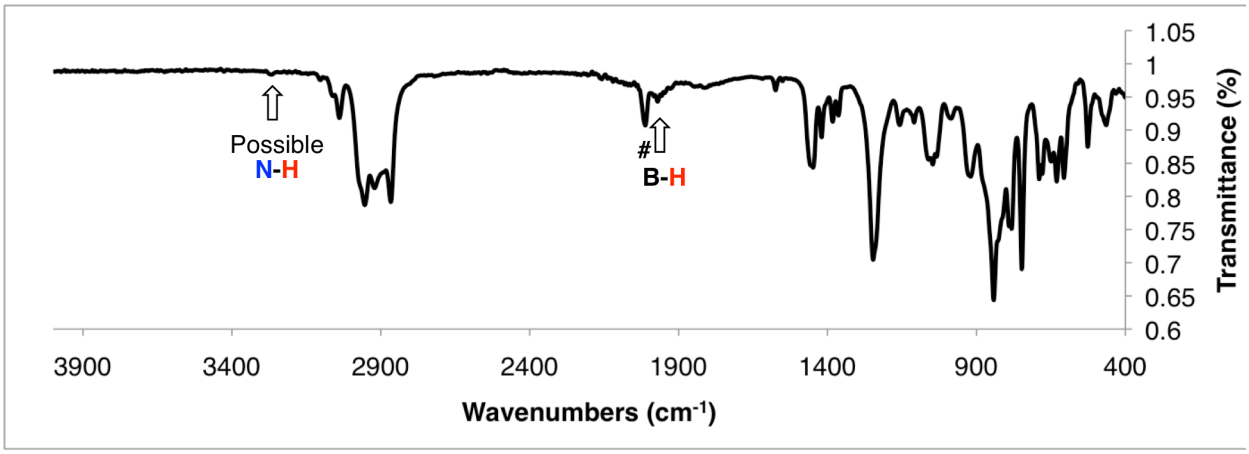

Figure S30. IR spectrum of $P_3^B(\mu\text{-D})Fe(NDNSi_2)$ **8-D_2** (thin film). The presence of a minor N_2 containing impurity from an oxidation side reaction is indicated by #.

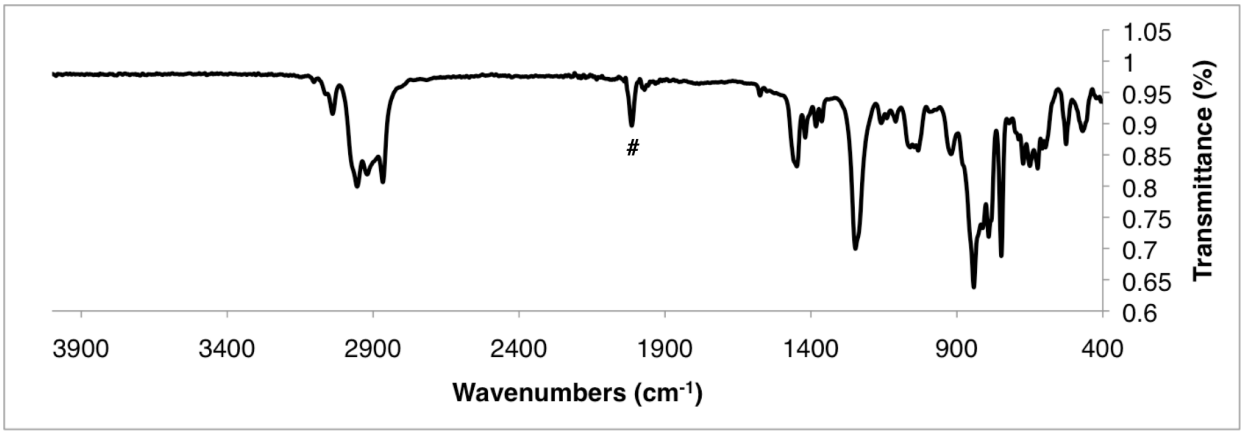

Figure S31. IR spectrum of $P_3^B(\mu\text{-H})Fe(NHNSi_2)(CN^tBu)$ **9** (thin film from C_6D_6).

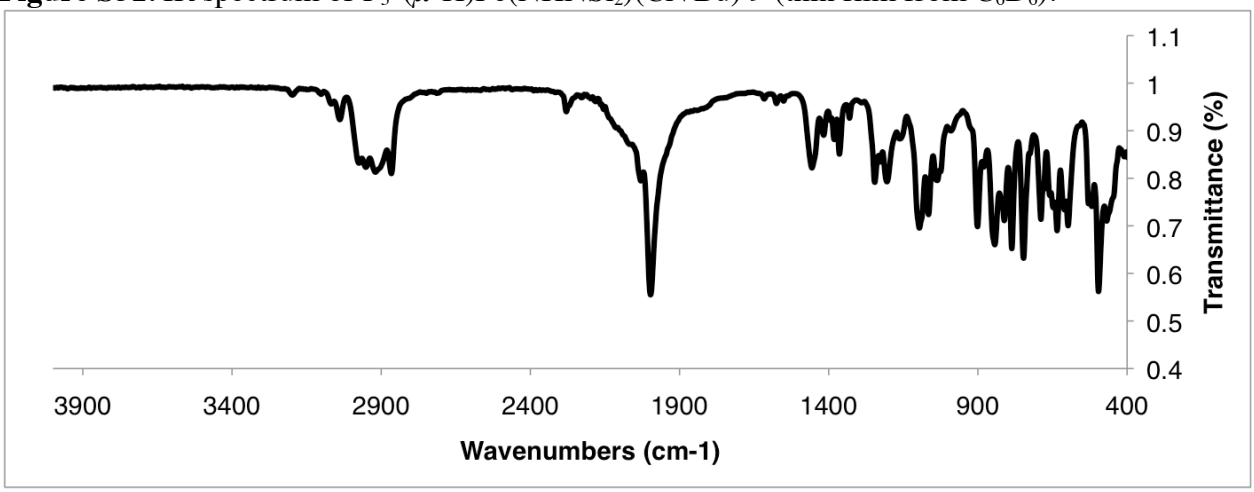

Figure S32. IR spectrum of $P_3^B(\mu\text{-D})Fe(NDNSi_2)(CN^tBu)$ **9-D$_2$** (thin film from C_6D_6)

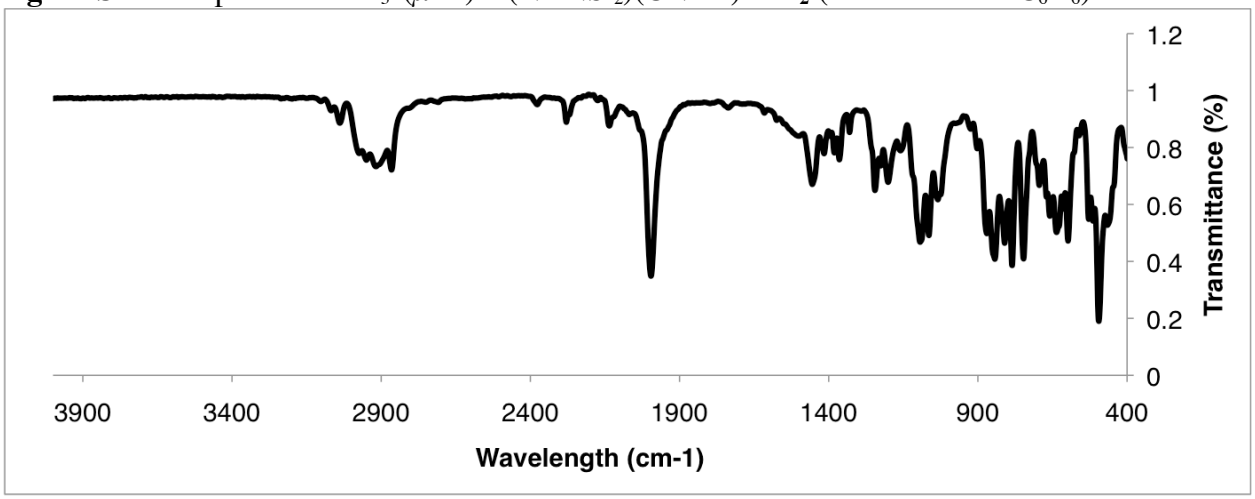

Figure S33. IR spectrum of $[(P_3^B\text{-H})Fe(CN^tBu)][B(C_8H_3F_6)_4]$ (thin film from THF-d_8).

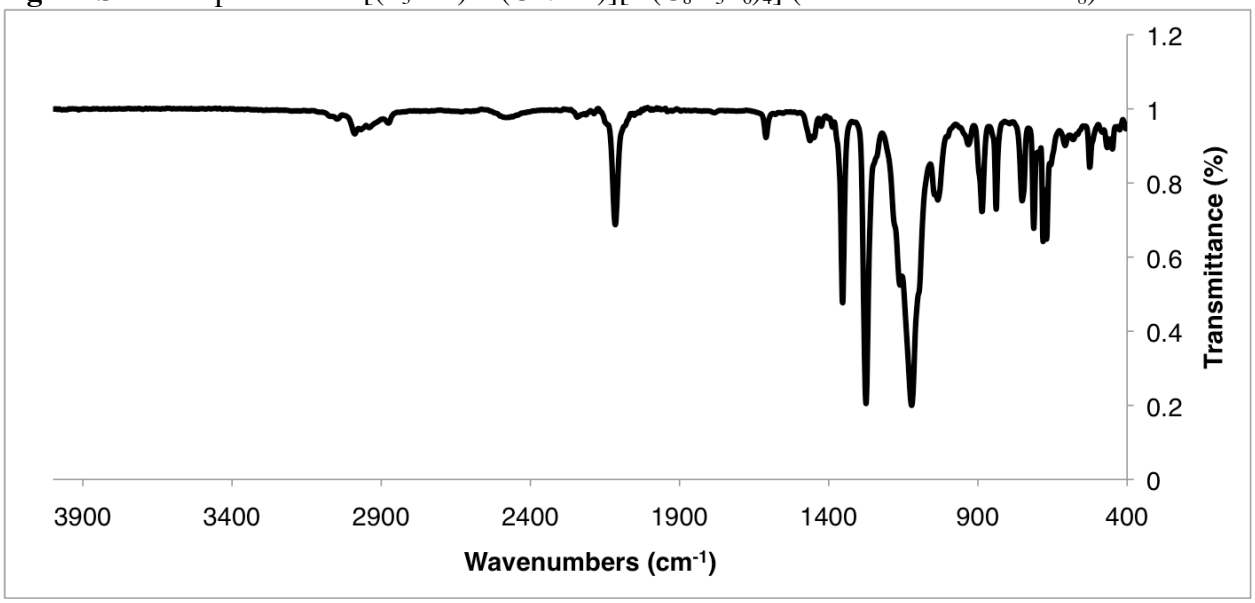

5. UV-vis Spectra

Figure S34. UV-vis spectrum of $[P_3^B(\mu\text{-H})Fe(H)(N_2)][K_2(THF)_n]$ **2** (3.2 x 10^{-4} mM) in THF.

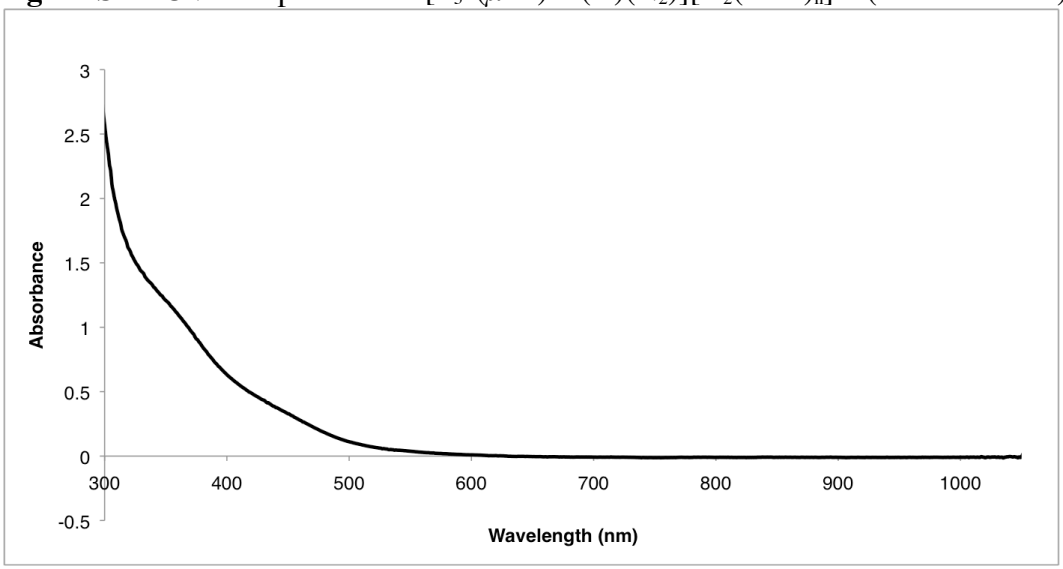

Figure S35. UV-vis spectrum of $[P_3^BFe(H)(N_2)][K(benzo\text{-}15\text{-}crown\text{-}5)_2]$ **4** in THF.

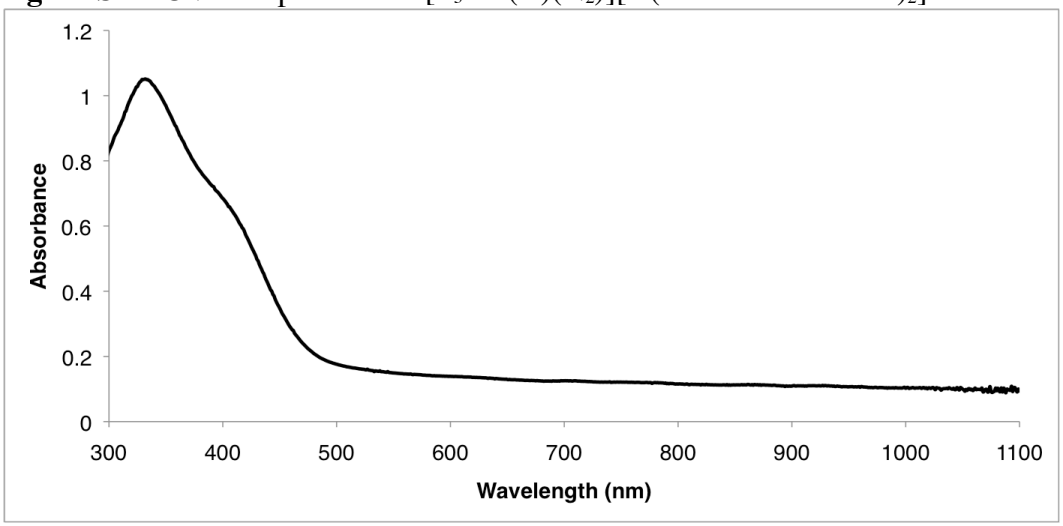

Figure S36. UV-vis spectrum of $P_3^B(\mu\text{-H})Fe(H)(NNSi_2)$ **7** at -78 °C in THF.

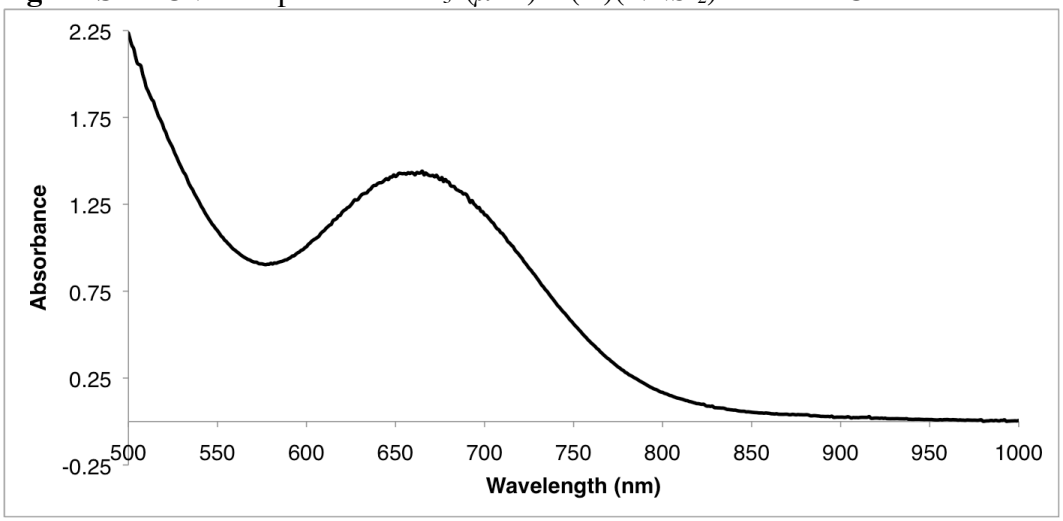

Figure S37. UV-vis spectrum of $P_3^B(\mu\text{-H})Fe(NHNSi_2)(CN^tBu)$ **9** in THF.

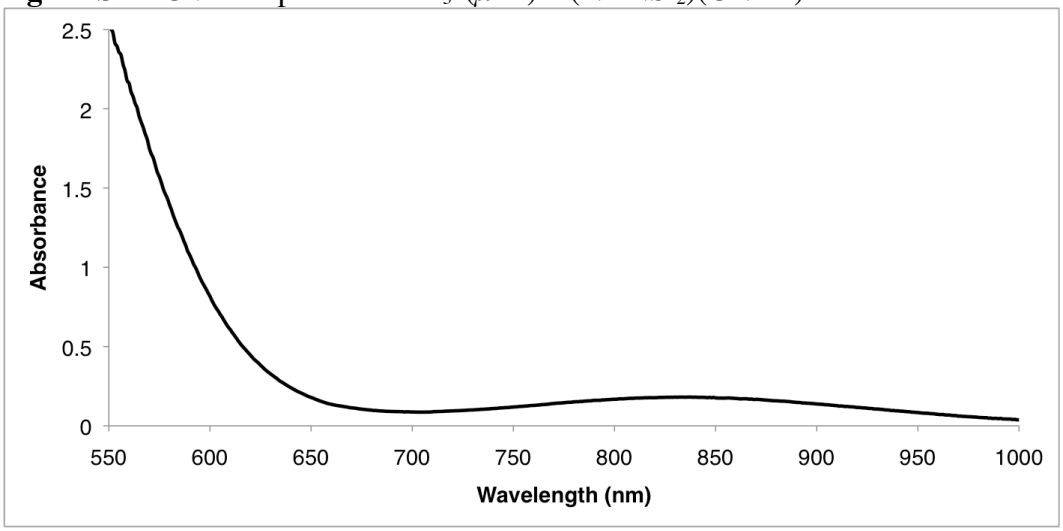

Figure S38. UV-vis spectrum of $[(P_3^B\text{-H})Fe(CN^tBu)][BAr^F{}_4]$ in THF.

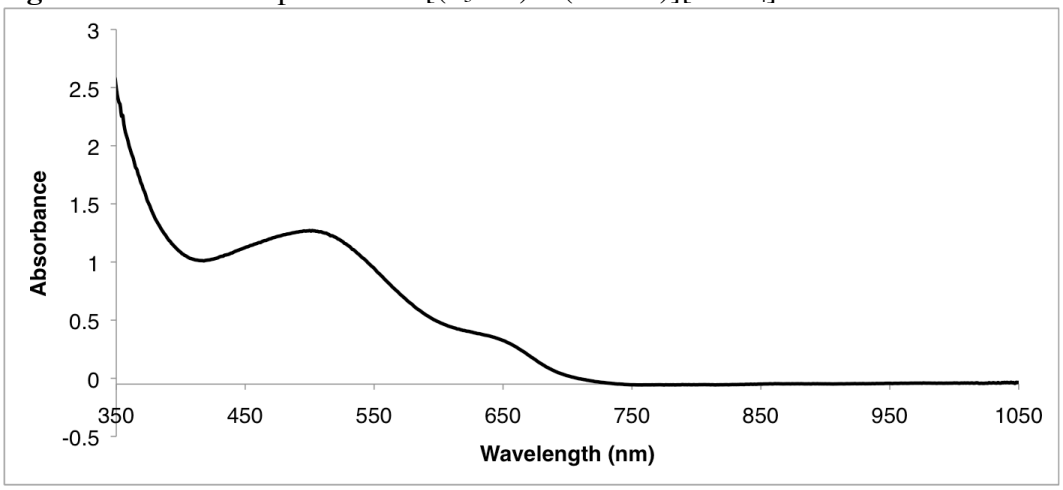

6. Mössbauer Spectra

Figure S39. Mössbauer spectrum of $[P_3^B(\mu\text{-H})Fe(H)(N_2)][K_2(THF)_n]$ **2** collected at 80 K in THF (δ = 0.25; ΔE_Q = 2.28). The residual impurity signal (δ = 0.30; ΔE_Q = 0.73) is likely due to oxidation during sample preparation.

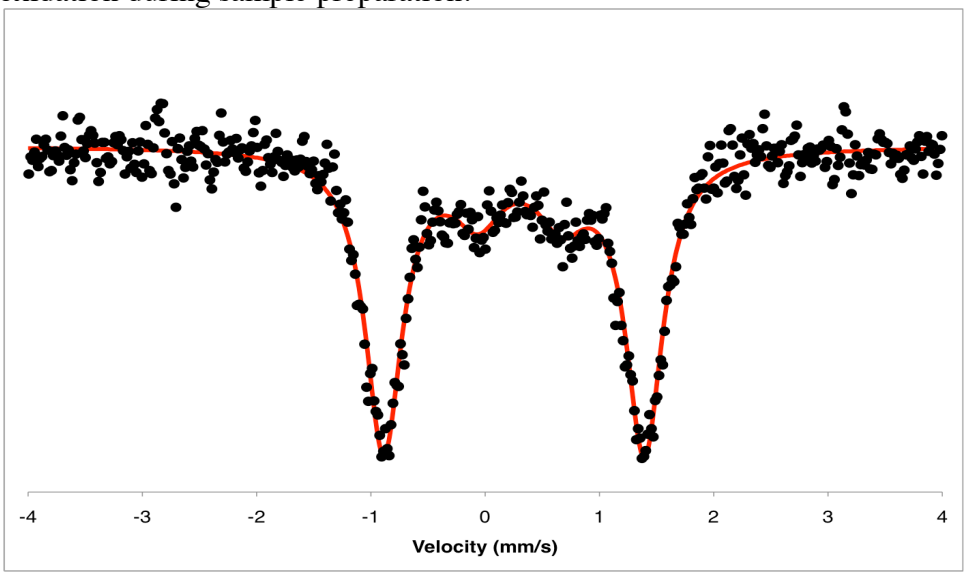

Figure S40. Mössbauer spectrum of $[P_3^BFe(H)(N_2)][K(benzo\text{-}15\text{-}crown\text{-}5)_2]$ **5** collected at 80 K in THF. (δ = 0.20; ΔE_Q = 0.84)

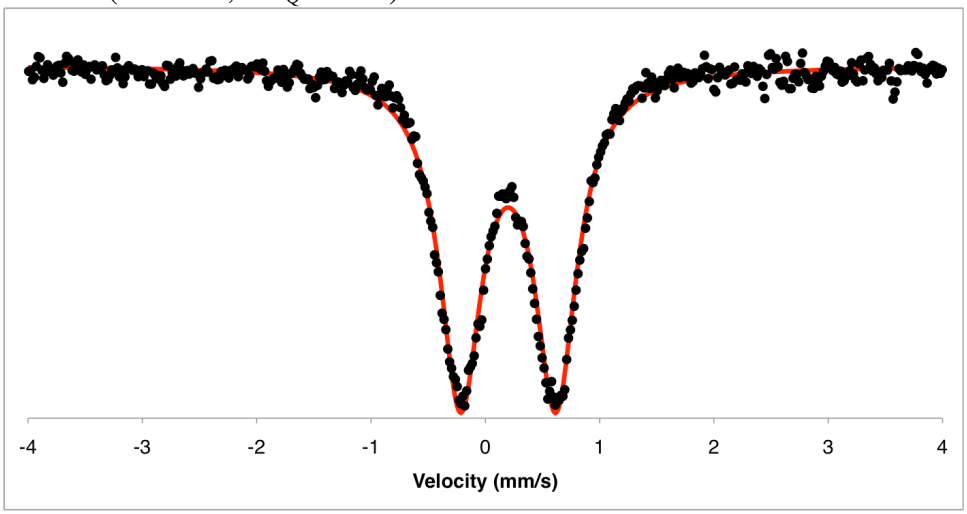

7. Kinetic Experiments

For kinetic analysis of the N-H bond forming step in the transformation of **7** to **8**, solutions of **7** were prepared *in situ* at -78 °C according to the procedure detailed in section 1 above and diluted to typical concentrations on the order of 5-9 mM, which allowed for convenient kinetic analysis by following the decay of the absorption at 660 nm ($\varepsilon \approx 240\ M^{-1}cm^{-1}$) in the UV-visible spectrum for the intermediate species **7**, which exhibited clean, isosbestic behavior. Following generation of the species **7** at low temperature, its clean generation was confirmed by UV-Vis analysis at -78 °C. Subsequently, the spectrometer was equilibrated to the desired reaction temperature (-15-20 °C) and the solutions were equilibrated to the reaction temperature over five minutes prior to initiating data collection. Attempts to obtain meaningful kinetic data at higher reaction temperatures were complicated by the competitive decay of the product **8**.

Because of our inability to isolate the starting material and products, extraction of rate constants from raw data was carried out using a method based on the use of difference equations.

For a general 1st order reaction:

a) $A_{\lambda,\infty} - A_{\lambda,t} = (A_{\lambda,\infty} - A_{\lambda,0})e^{-kt}$
b) $A_{\lambda,\infty} - A_{\lambda,t+\Delta t} = (A_{\lambda,\infty} - A_{\lambda,0})e^{-k(t+\Delta t)}$

Taking the difference gives:

$A_{\lambda,t+\Delta t} - A_{\lambda,t} = (A_{\lambda,\infty} - A_{\lambda,0})e^{-kt}(1-e^{-k\Delta t})$

So, with minor manipulation:

$A_{\lambda,t+\Delta t} = A_{\lambda,t}e^{-k\Delta t} + A_{\lambda,\infty}(1-e^{-k\Delta t})$

And a plot of $A_{\lambda,t}$ vs. $A_{\lambda,t+\Delta t}$ is linear with a slope of $e^{-k\Delta t}$: $k = -\ln(m)/(\Delta t)$

The linearity of the data extracted using this analysis confirms the first order nature of this transformation, with significant deviations from linearity expected for higher order reactions.

Figure S41. Representative UV-Vis spectrum for transformation of 7 to 8 (10 °C; Δt = 360).

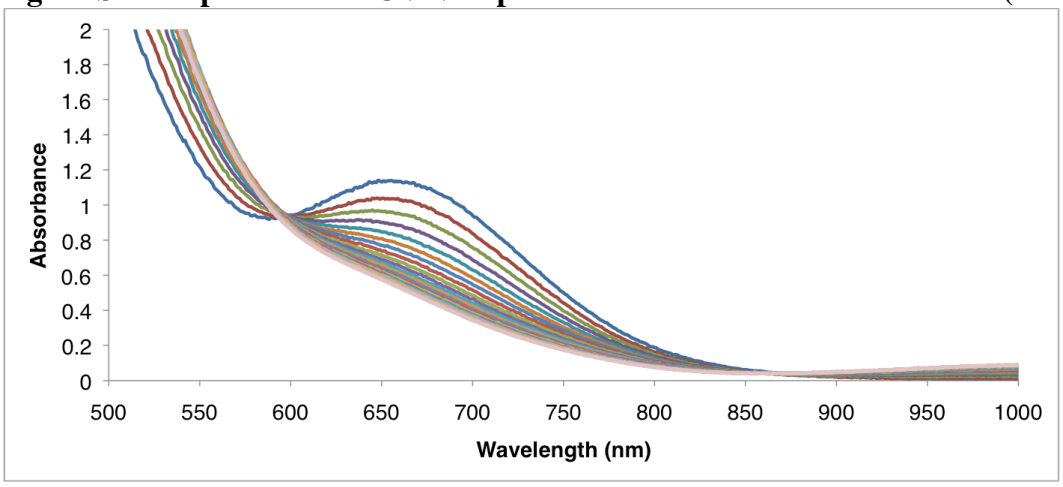

Figure S42. Plot of $A_{\lambda,t}$ vs. $A_{\lambda,t+\Delta t}$ at -15 °C (Run 1; 660 nm; Δt = 600 s; k = 2.40 x 10^{-5} s^{-1}).

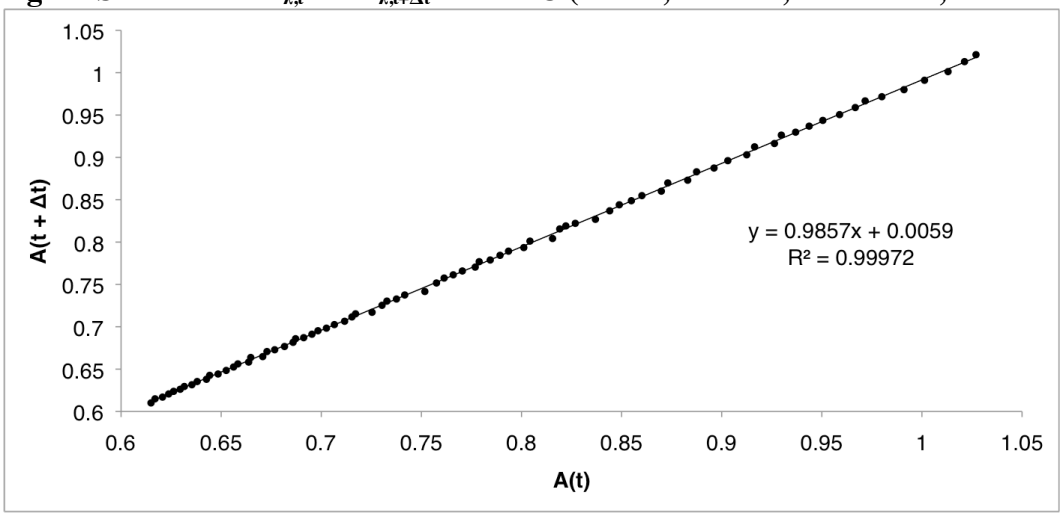

Figure S43. Plot of $A_{\lambda,t}$ vs. $A_{\lambda,t+\Delta t}$ at -15 °C (Run 2; 660 nm; Δt = 600 s; k = 2.77 x 10^{-5} s^{-1}).

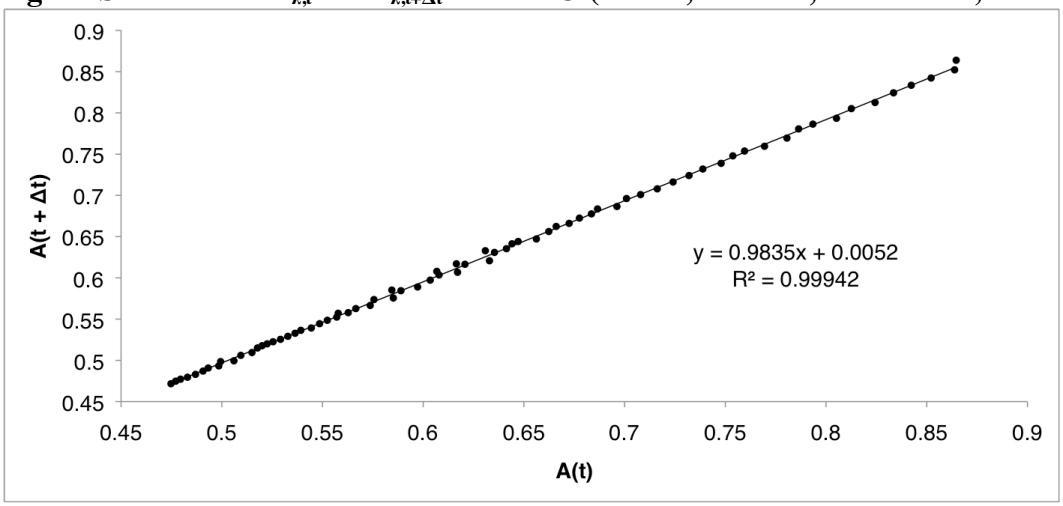

Figure S44. Plot of $A_{\lambda,t}$ vs. $A_{\lambda,t+\Delta t}$ at -10 °C (Run 1; 660 nm; Δt = 300 s; k = 4.23 x 10^{-5} s^{-1}).

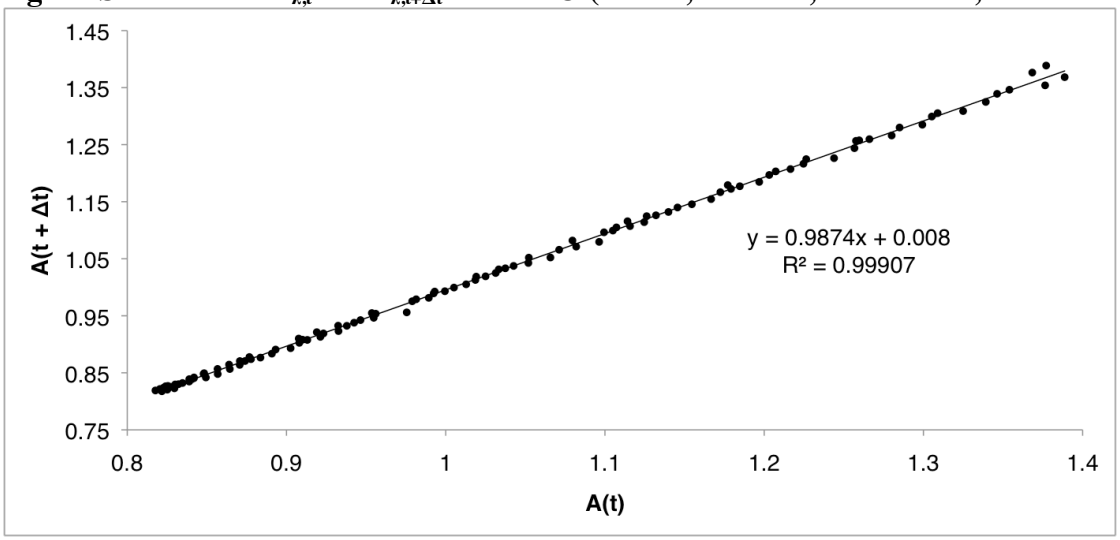

Figure S45. Plot of $A_{\lambda,t}$ vs. $A_{\lambda,t+\Delta t}$ at -10 °C (Run 2; 660 nm; Δt = 600 s; k = 4.84 x 10^{-5} s^{-1}).

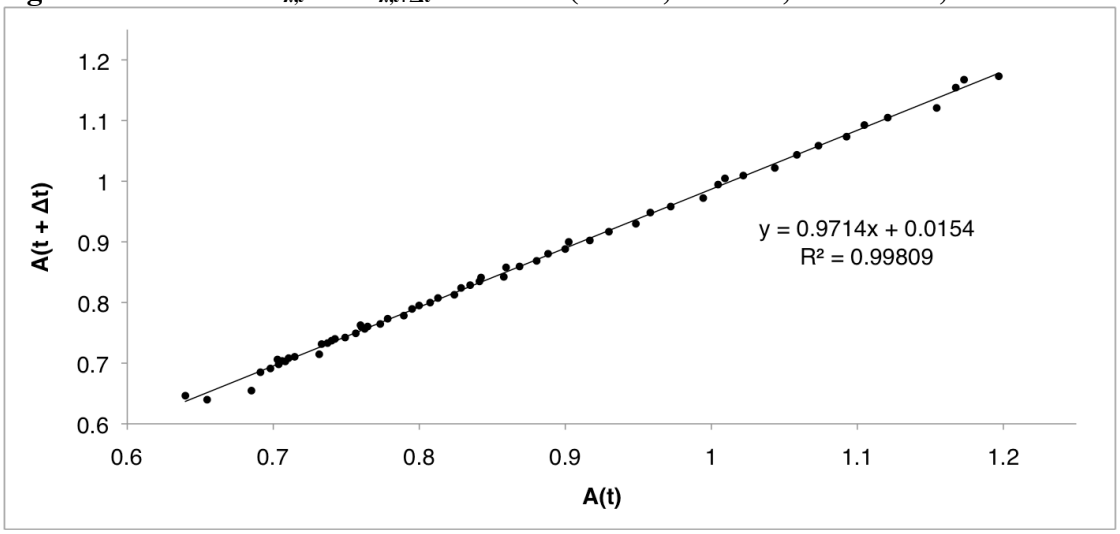

Figure S46. Plot of $A_{\lambda,t}$ vs. $A_{\lambda,t+\Delta t}$ at -5 °C (Run 1; 660 nm; Δt = 300 s; k = 1.05 x 10^{-4} s^{-1}).

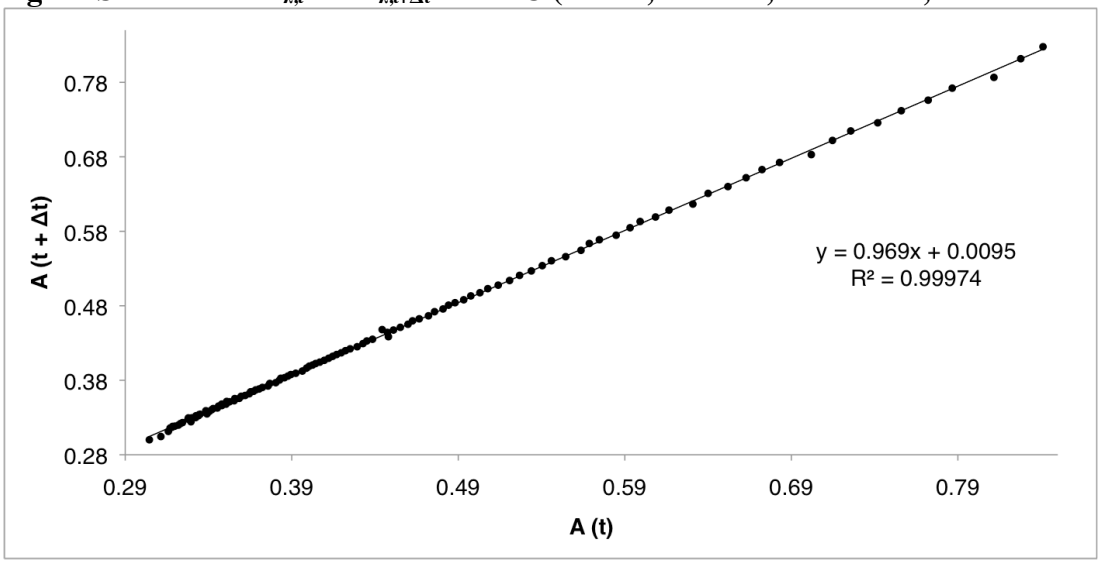

Figure S47. Plot of $A_{\lambda,t}$ vs. $A_{\lambda,t+\Delta t}$ at -5 °C (Run 2; 660 nm; Δt = 300 s; k = 8.51 x 10^{-5} s^{-1}).

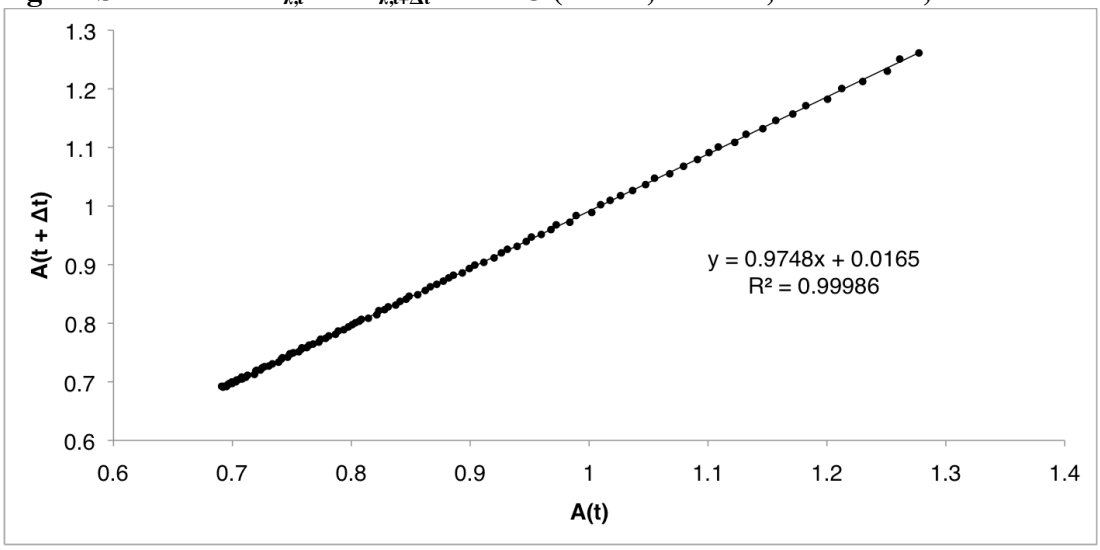

Figure S48. Plot of $A_{\lambda,t}$ vs. $A_{\lambda,t+\Delta t}$ at 0 °C (Run 1; 660 nm; Δt = 120 s; k = 1.65 x 10^{-4} s^{-1}).

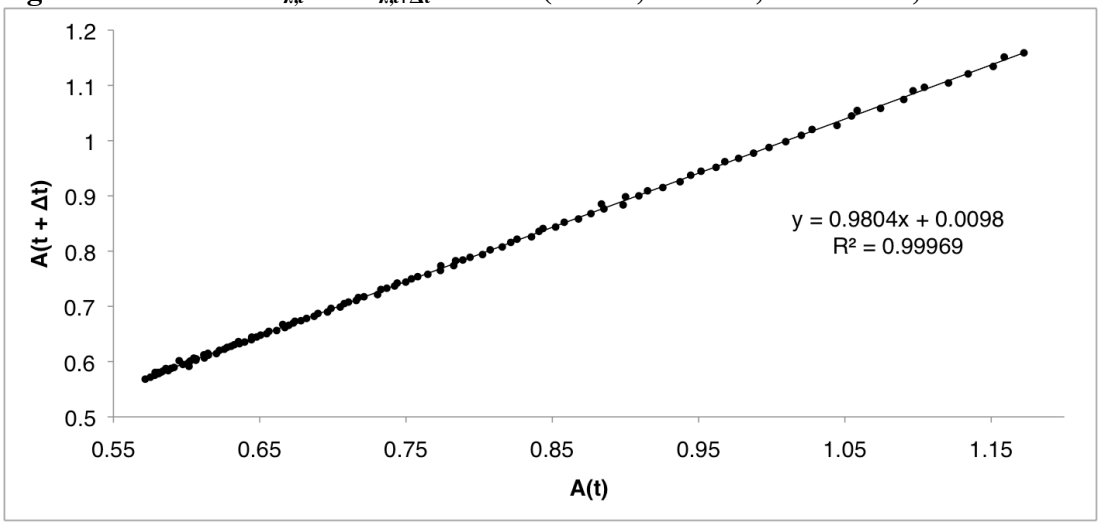

Figure S49. Plot of $A_{\lambda,t}$ vs. $A_{\lambda,t+\Delta t}$ at 0 °C (Run 2; 660 nm; Δt = 300 s; k = 1.54 x 10^{-4} s^{-1}).

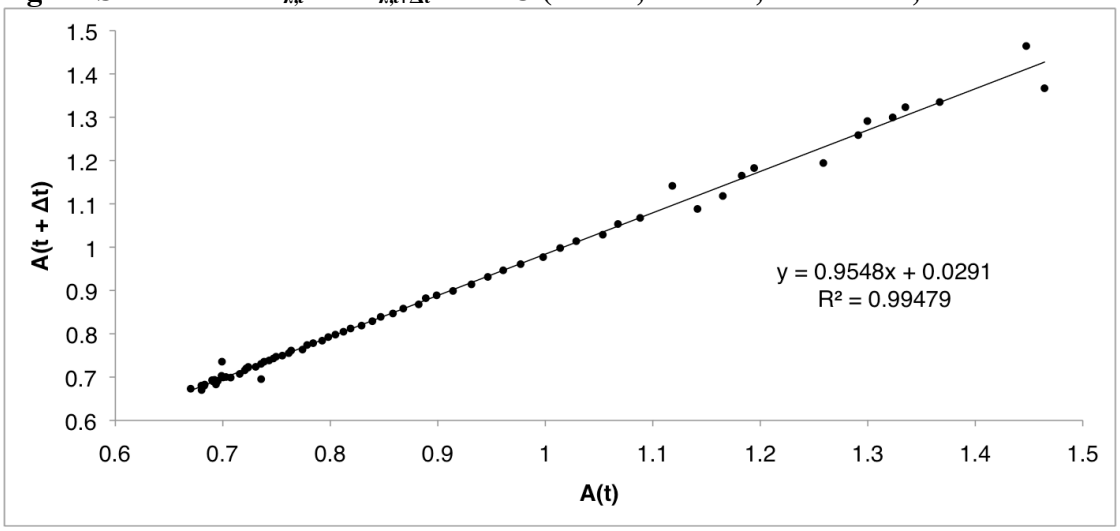

Figure S50. Plot of $A_{\lambda,t}$ vs. $A_{\lambda,t+\Delta t}$ at 5 °C (Run 1; 660 nm; Δt = 120 s; k = 3.00 x 10^{-4} s^{-1}).

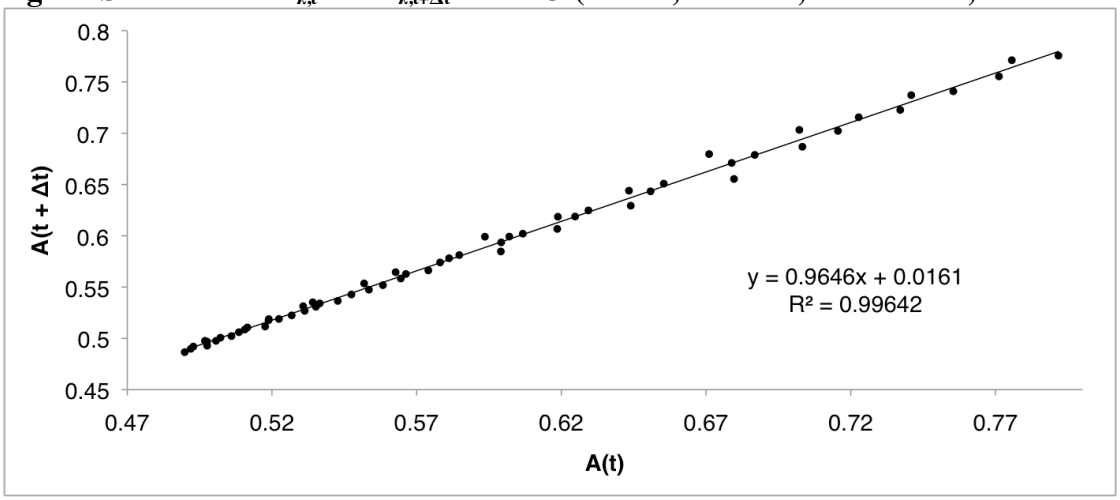

Figure S51. Plot of $A_{\lambda,t}$ vs. $A_{\lambda,t+\Delta t}$ at 5 °C (Run 2; 660nm; Δt = 120 s; k = 3.29 x 10^{-4} s^{-1}).

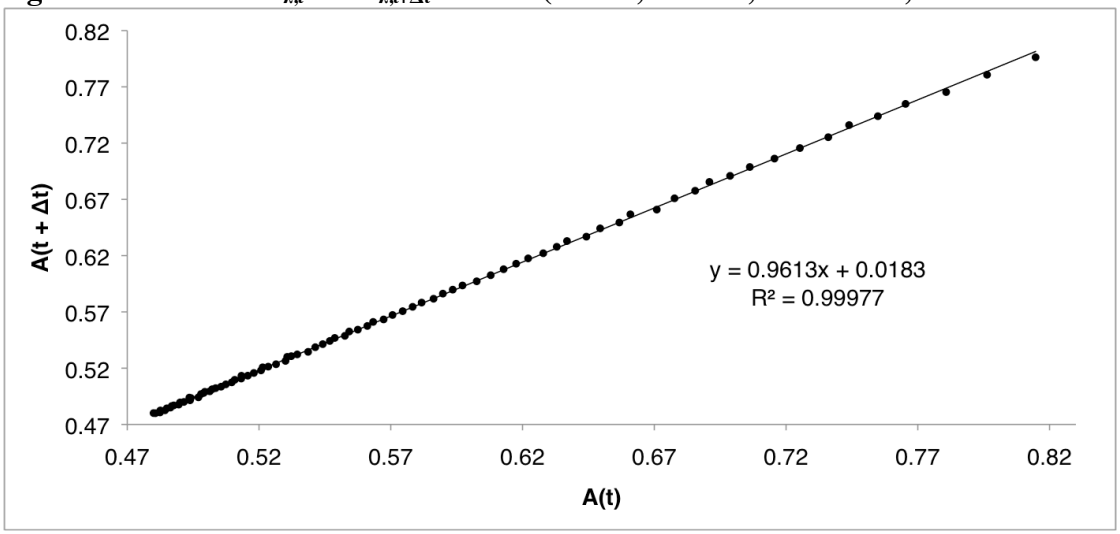

Figure S52. Plot of $A_{\lambda,t}$ vs. $A_{\lambda,t+\Delta t}$ at 10 °C (Run 1; 660nm; Δt = 360 s; k = 4.98 x 10^{-4} s^{-1}).

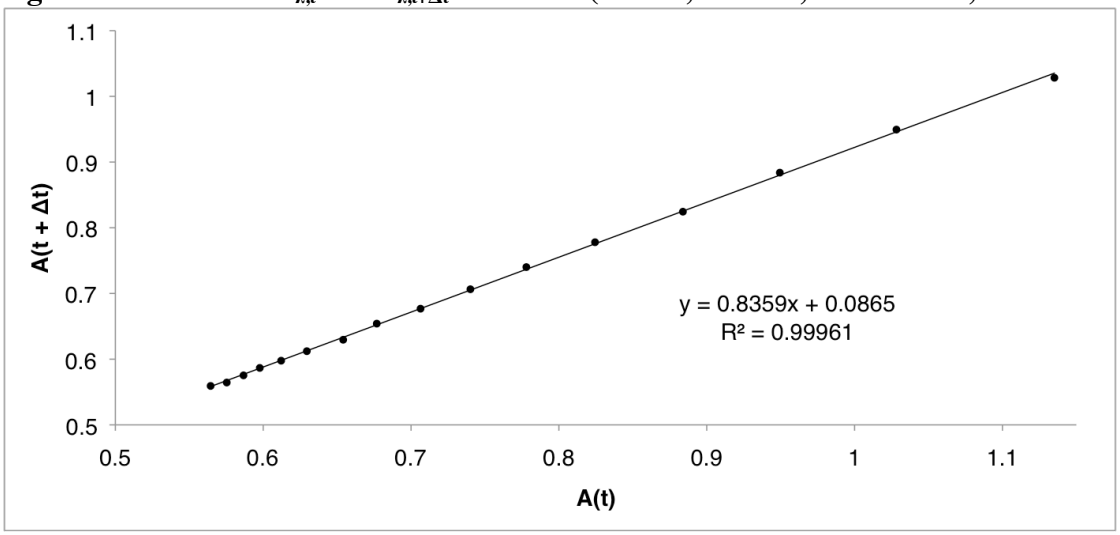

Figure S53. Plot of $A_{\lambda,t}$ vs. $A_{\lambda,t+\Delta t}$ at 10 °C (Run 2; 660nm; Δt = 120 s; k = 4.20 x 10^{-4} s^{-1}).

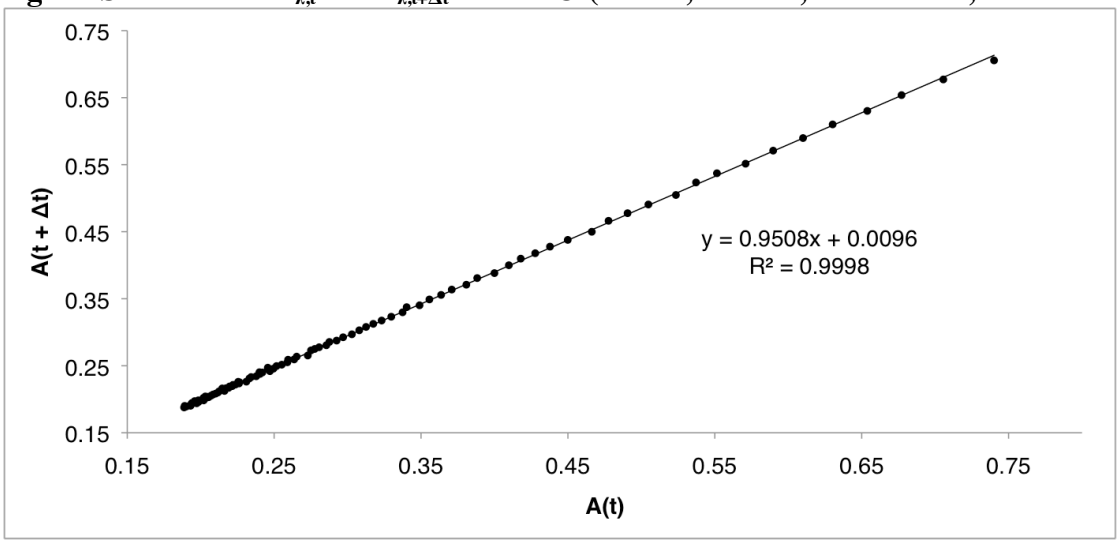

Figure S54. Plot of $A_{\lambda,t}$ vs. $A_{\lambda,t+\Delta t}$ at 15 °C (Run 1; 660nm; Δt = 60 s; k = 8.60 x 10^{-4} s^{-1}).

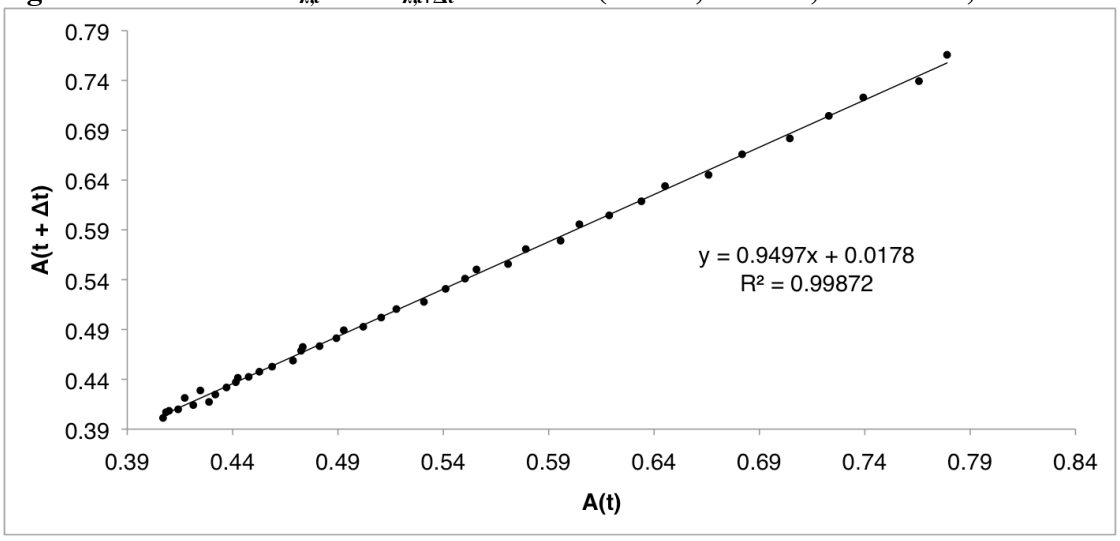

Figure S55. Plot of $A_{\lambda,t}$ vs. $A_{\lambda,t+\Delta t}$ at 15 °C (Run 2; 660nm; Δt = 60 s; k = 8.15 x 10^{-4} s^{-1}).

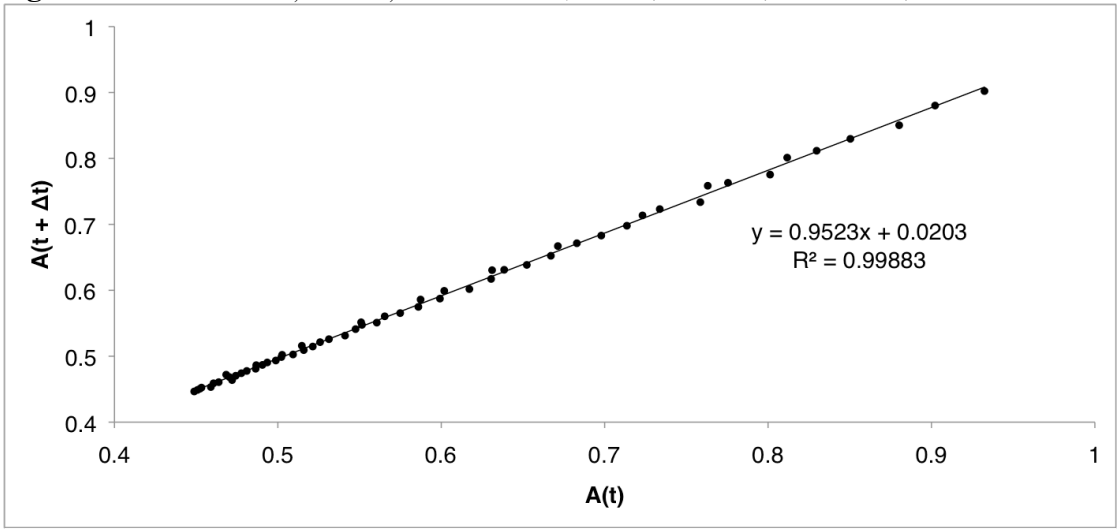

Figure S56. Plot of $A_{\lambda,t}$ vs. $A_{\lambda,t+\Delta t}$ at 20 °C (Run 1; 660nm; Δt = 120 s; k = 1.40 x 10^{-3} s^{-1}).

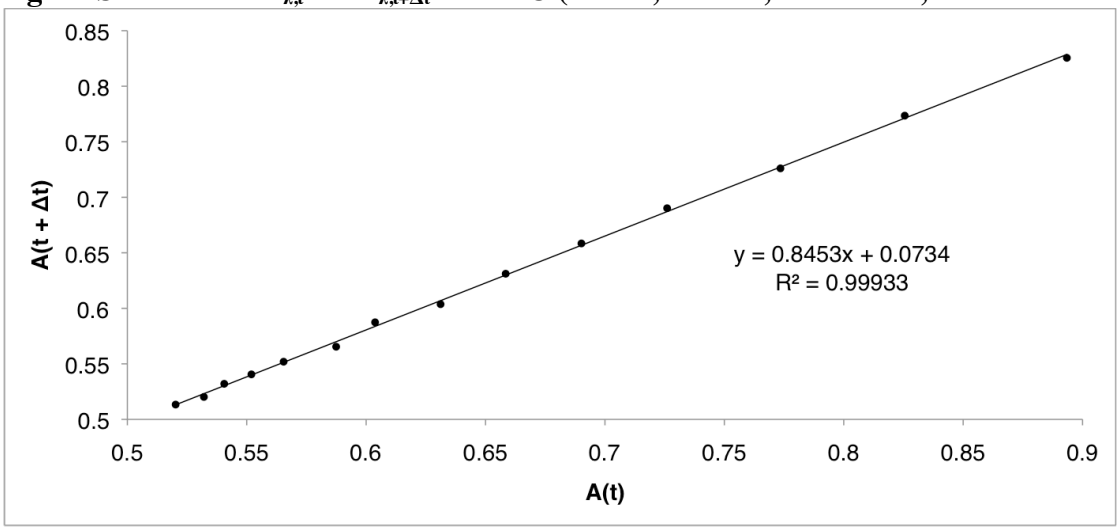

Figure S57. Plot of $A_{\lambda,t}$ vs. $A_{\lambda,t+\Delta t}$ at 20 °C (Run 2; 660nm; Δt = 60 s; k = 1.68 x 10^{-3} s^{-1}).

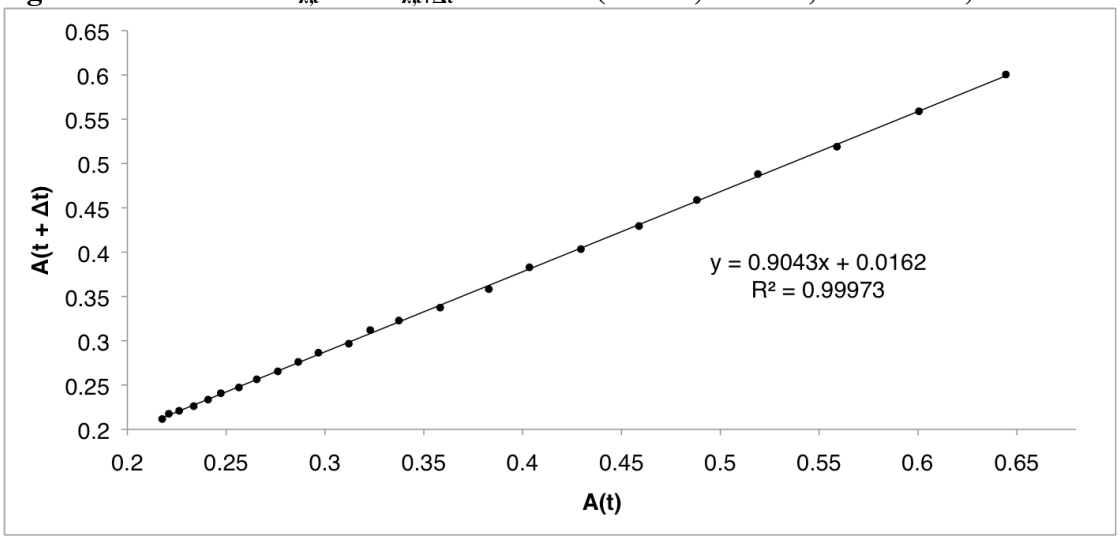

Table S1. Rate Constants for the Decay of 7 to 8

Temperature (K)	Run 1 (s^{-1})	Run 2 (s^{-1})	Average (s^{-1})	Std. Dev. (s^{-1})
258	2.40 x 10^{-5}	2.77 x 10^{-5}	2.59 x 10^{-5}	2.63 x 10^{-6}
263	4.23 x 10^{-5}	4.84 x 10^{-5}	4.54 x 10^{-5}	4.31 x 10^{-6}
268	1.05 x 10^{-4}	8.51 x 10^{-5}	9.50 x 10^{-5}	1.41 x 10^{-5}
273	1.65 x 10^{-4}	1.54 x 10^{-4}	1.60 x 10^{-4}	7.78 x 10^{-6}
278	3.00 x 10^{-4}	3.29 x 10^{-4}	3.15 x 10^{-4}	2.02 x 10^{-5}
283	4.98 x 10^{-4}	4.20 x 10^{-4}	4.59 x 10^{-4}	5.52 x 10^{-5}
288	8.60 x 10^{-4}	8.15 x 10^{-4}	8.37 x 10^{-4}	3.22 x 10^{-5}
293	1.40 x 10^{-3}	1.68 x 10^{-3}	1.54 x 10^{-3}	1.98 x 10^{-4}

Figure S58. Eyring Plot for the Decay of 7 to 8. ($\Delta H^{\ddagger}$ = 16.8; $\Delta S^{\ddagger}$ = -14.0).

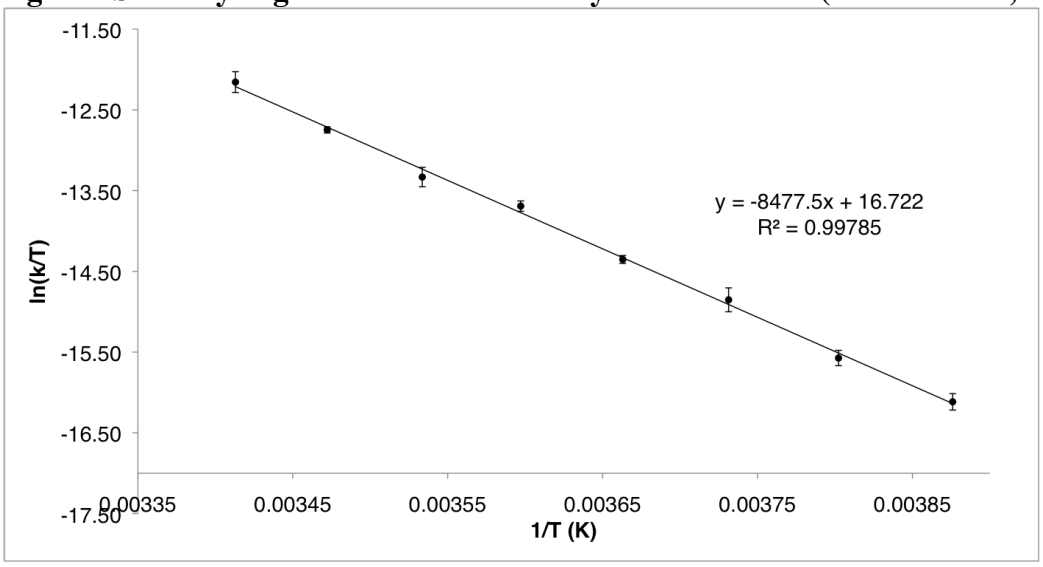

Figure S59. Plot of $A_{\lambda,t}$ vs. $A_{\lambda,t+\Delta t}$ at 10 °C (Run 1; 660nm; D_2; Δt = 120 s; k = 3.47 x 10^{-4} s^{-1}).

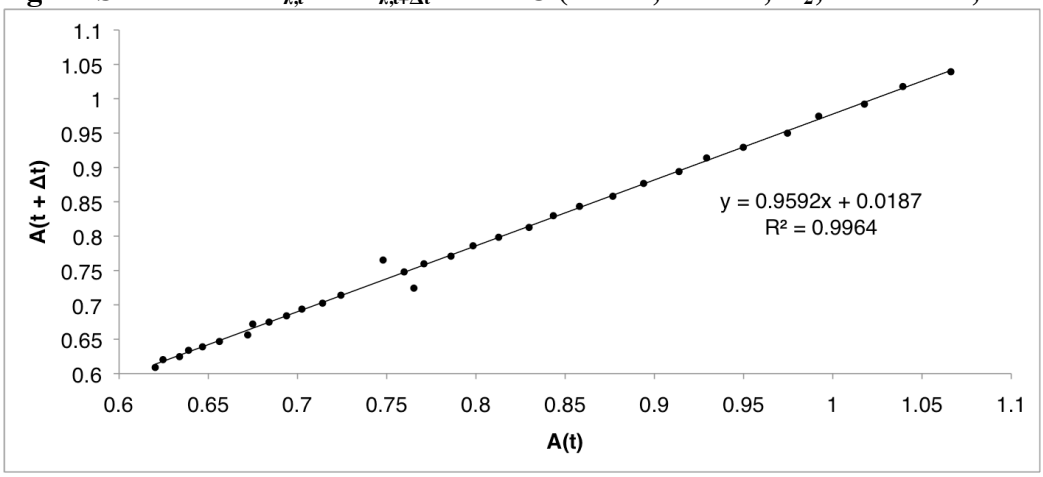

Figure S60. Plot of $A_{\lambda,t}$ vs. $A_{\lambda,t+\Delta t}$ at 10 °C (Run 2; 660nm; D_2; Δt = 120 s; k = 3.47 x 10^{-4} s^{-1}).

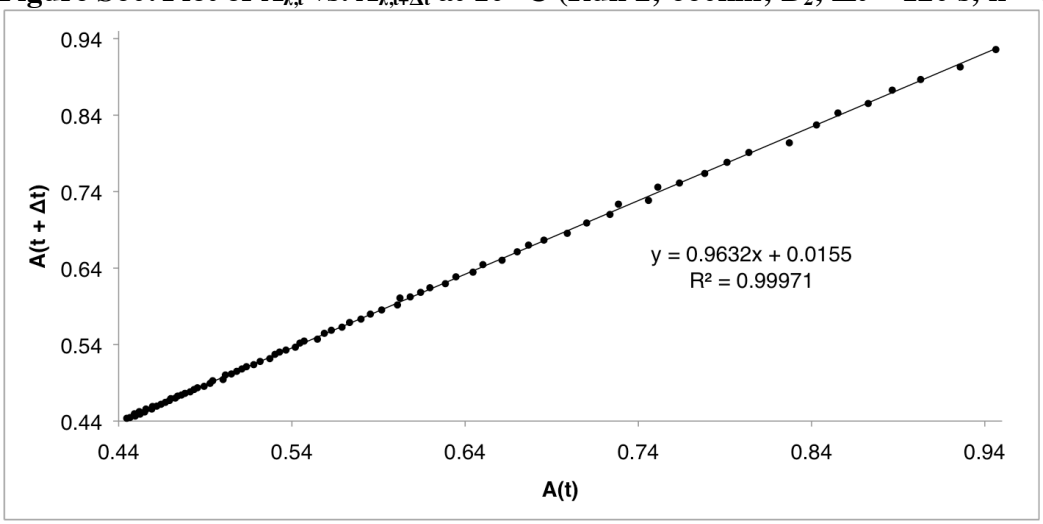

Table S2. Rate Constants for the Decay of 7 to 8 for Unlabeled and D_2-Labeled Complexes

	Run 1 (s^{-1})	Run 2 (s^{-1})	Average (s^{-1})
H_2 (Unlabeled)	4.98×10^{-4}	4.20×10^{-4}	4.59×10^{-4}
D_2 (Labeled)	3.47×10^{-4}	3.12×10^{-4}	3.30×10^{-4}
KIE			1.39

8. Additional Experiments

8.1. Reactivity of [$P_3^BFe(N_2)(H)$][K(benzo-15-crown-5)$_2$] 4

Oxidation: We explored conditions to access the neutral hydride complex (P_3^B-H)Fe(N_2), where the analogous CO complex has been reported.[7] Treatment of the anionic hydride complex **4** with [Cp_2Co][PF_6] at -78 °C in THF provides access to a new doublet species, which we have tentatively assigned as (P_3^B-H)Fe(N_2). This species has a broad, paramagnetically wshifted ^{1}H NMR spectrum, with B-H and Fe-N_2 stretches observed at 2590 cm^{-1} and 2011 cm^{-1} respectively in its IR spectrum. This N_2 stretch is identical to its neutral hydride-free counterpart **3**, though is distinguished by its greater intensity and the unique B-H stretch. The analogous CO complexes P_3^BFe(CO)[8] and (P_3^B-H)Fe(CO) also have quite similar CO stretching frequencies, which are reported to be 1857 cm^{-1} and 1862 cm^{-1} respectively and the latter having a similar B-H stretch to (P_3^B-H)Fe(N_2) at 2588 cm^{-1}. The Mössbauer spectrum of **5** exhibits an asymmetric quadrupole doublet with an isomer shift (δ = 0.42) and quadrupole splitting (ΔE_Q = 0.93) consistent with typical doublet species on this scaffold. Unfortunately, P_3^BFe species, because of the similar isomer shifts and quadrupole splittings of doublet species supported by this ligand scaffold, as well as the broad nature of their signals, it can be difficult to assign the purity of these species solely by the 77 K Mössbauer spectrum. It is clearly distinguished from the hydride-free N_2 complex, which has Mössbauer spectrum with a higher isomer shift (δ = 0.56) and much wider quadrupole splitting (ΔE_Q = 3.34).[9] The EPR spectrum of the reaction mixture appears to be most consistent with the presence of a mixture of species. Attempts to crystallographically characterize either of these neutral complexes have been unsuccessful, with problematic twinning reported in the case of complex **3**[8] and the complex generated upon oxidation of **4** observed to decay to P_3^BFe(N_2) in solution over time.

Figure S61. ^{1}H NMR (C_6D_6; 300 MHz) spectrum generated from the oxidation of **4** with [Cp_2Co][PF_6].

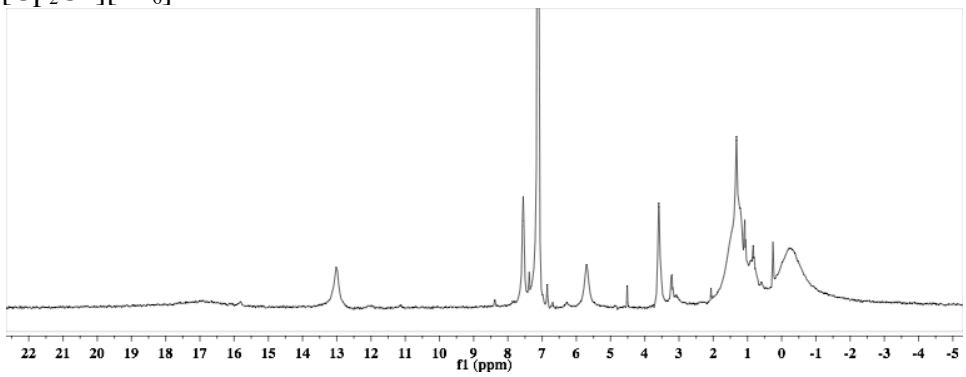

(7) M. M. Deegan, and J. C. Peters, *J. Am. Chem. Soc.*, 2017, **139**, 2561.
(8) M.-E. Moret, and J. C. Peters, *Angew. Chem. Int. Ed.*, 2011, **50**, 2063.
(9) J. S. Anderson, G. E. Cutsail, J. Rittle, B. A. Connor, W. A. Gunderson, L. Zhang, B. M. Hoffman, and J. C. Peters, *J. Am. Chem. Soc.*, 2015, **137**, 7803.

Figure S62. IR spectrum (thin film) of the oxidation product $(P_3^B\text{-H})Fe(N_2)$.

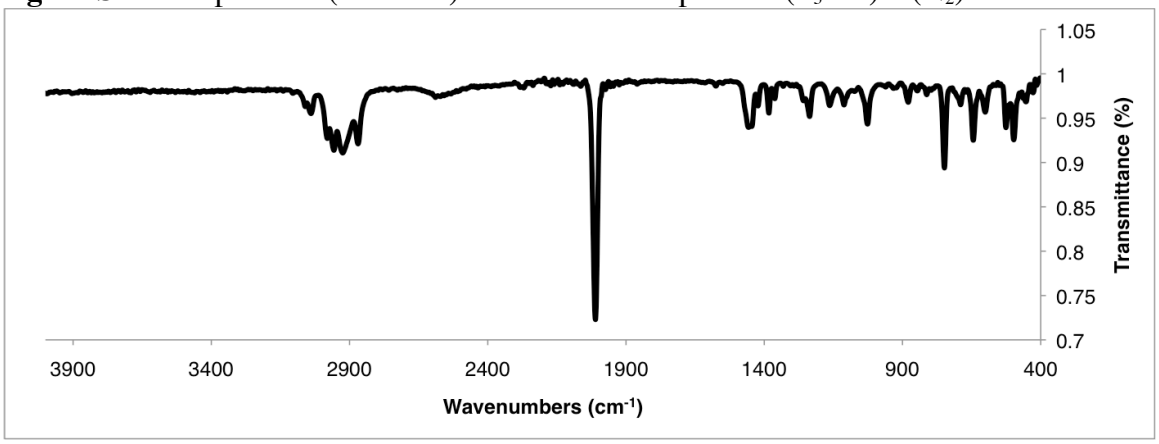

Figure S63. IR spectrum (thin film) of an authentic sample of $P_3^BFeN_2$.

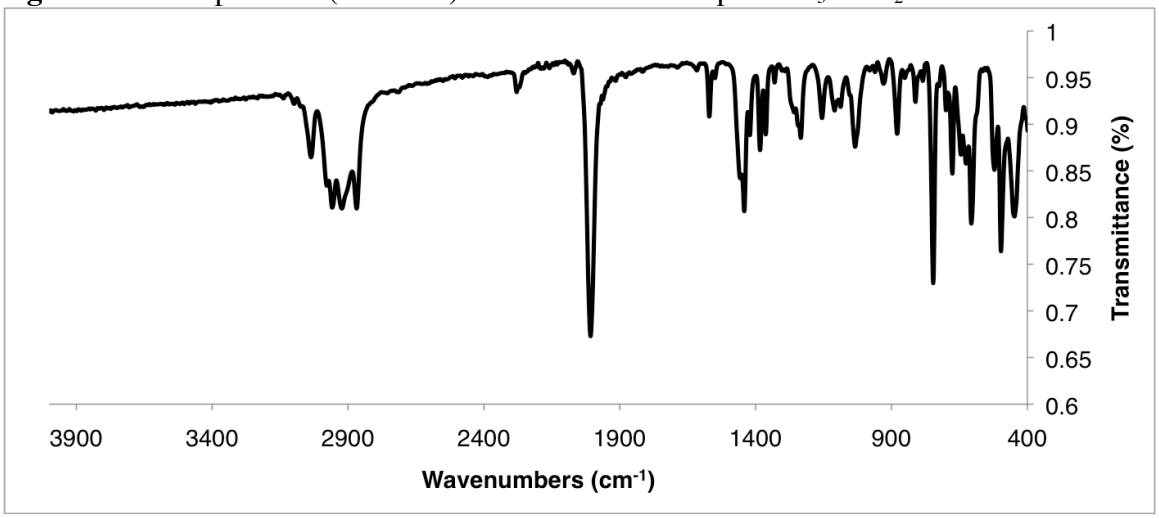

Figure S64. Mössbauer spectrum of $(P_3^B\text{-H})Fe(N_2)$ generated *in situ* ($\delta = 0.42$; $\Delta E_Q = 0.93$).

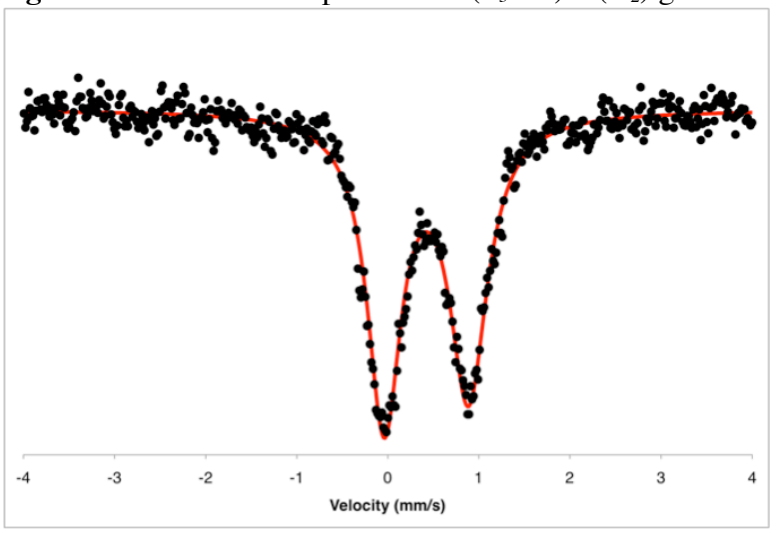

Figure S65. EPR spectrum of (P_3^B-H)Fe(N_2) generated *in situ*.

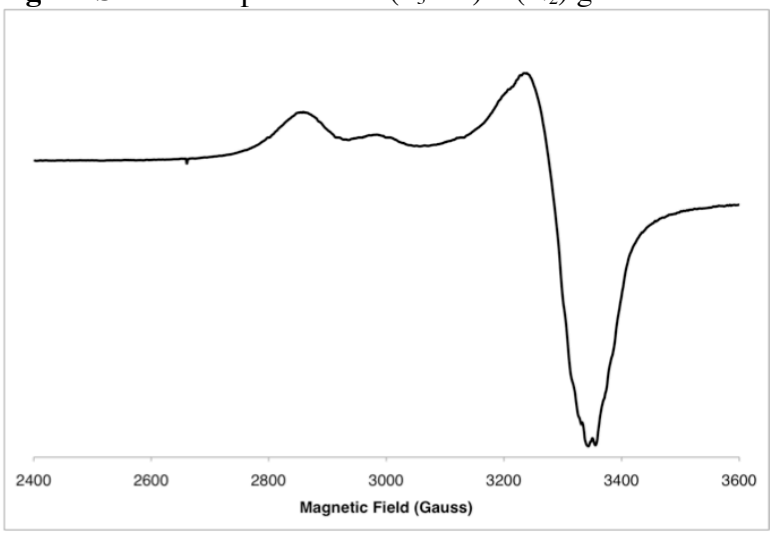

Functionalization: Treatment of the monoanionic complex **4** with a stoichiometric equivalent of trimethylsilyl triflate electrophile leads to the generation of a new species that can be observed at low temperature. By NMR spectroscopy, the product is a diamagnetic species that retains a hydride ligand that we have tentatively assigned as P_3^BFe(H)(NNSiMe_3). At room temperature, this compound decays to a mixture of identifiable species over time, including P_3^BFe(NNSiMe_3)[10], (P_3^B-H)Fe(N_2), P_3^BFe(N_2)[8] and P_3^BFe(OTf)[11].

Figure S66. ^{1}H NMR spectrum obtained in THF-d_8 at -20 °C of the initial reaction mixture (500 MHz).

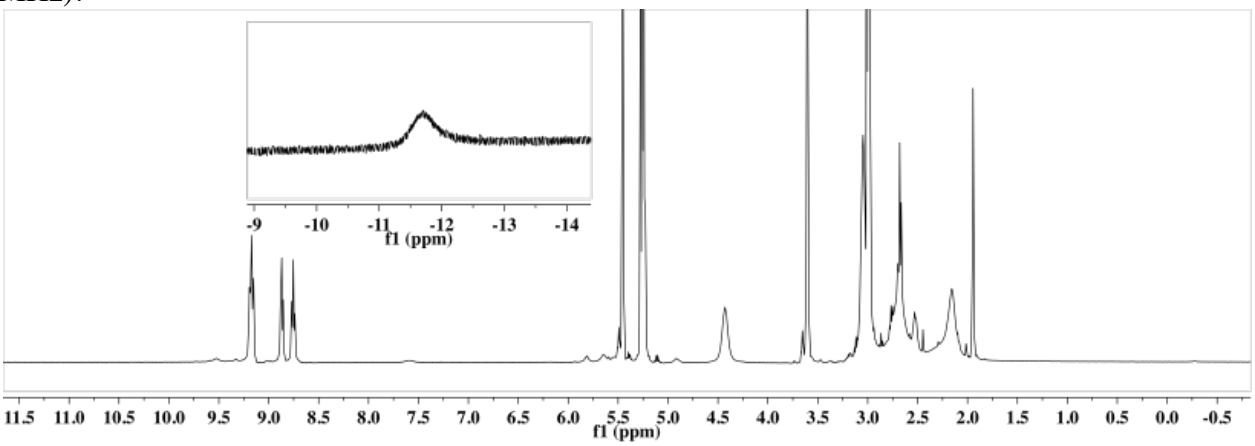

(10) M.-E. Moret, and J. C. Peters, *J. Am. Chem. Soc*., 2011, **133**, 18118.
(11) N. B. Thompson, M. T. Green, and J. C. Peters, *J. Am. Chem. Soc*., 2017, **139**, 15312.

Figure S67. ^{1}H NMR spectrum (THF-d_8; 500 MHz) showing the mixture of products appearing in the spectrum after warming to room temperature.

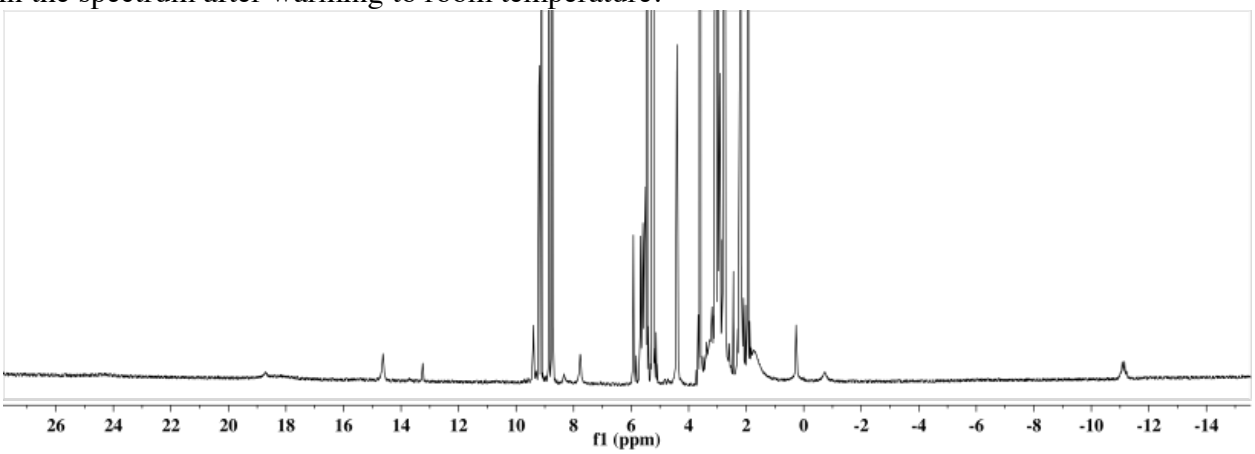

S.8.2 Additional Experiments Relevant to N-H Bond Formation

Reaction of **10-CN^{t}Bu** with H_2: The complex **10-CN^{t}Bu** was prepared according to a previously reported protocol.[12] A solution of this complex was prepared in benzene, degassed by one freeze-pump-thaw cycle, and exposed to an H_2 atmosphere overnight. After mixing for ~12 h, some decay of the starting material **10-CN^{t}Bu** was apparent, but the hydrazido(1-) complex **9** was not spectroscopically observed.

Figure S68. ^{31}P{^{1}H} NMR (C_6D_6; 162 MHz) Spectrum of **10-CN^{t}Bu** as prepared prior to exposure to H_2.

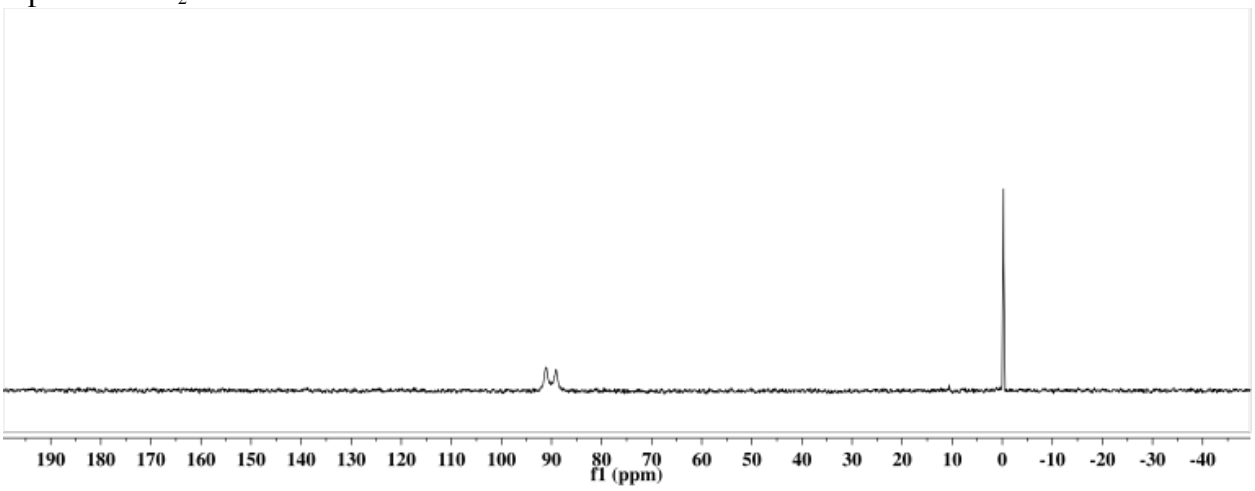

(12) M.-E. Moret, and J. C. Peters, *J. Am. Chem. Soc*., 2011, **133**, 18118.

Figure S69. ^{1}H NMR (C_6D_6; 400 MHz) spectrum of **10-CN^{t}Bu** as prepared prior to exposure to H_2 with a minor paramagnetic impurity.

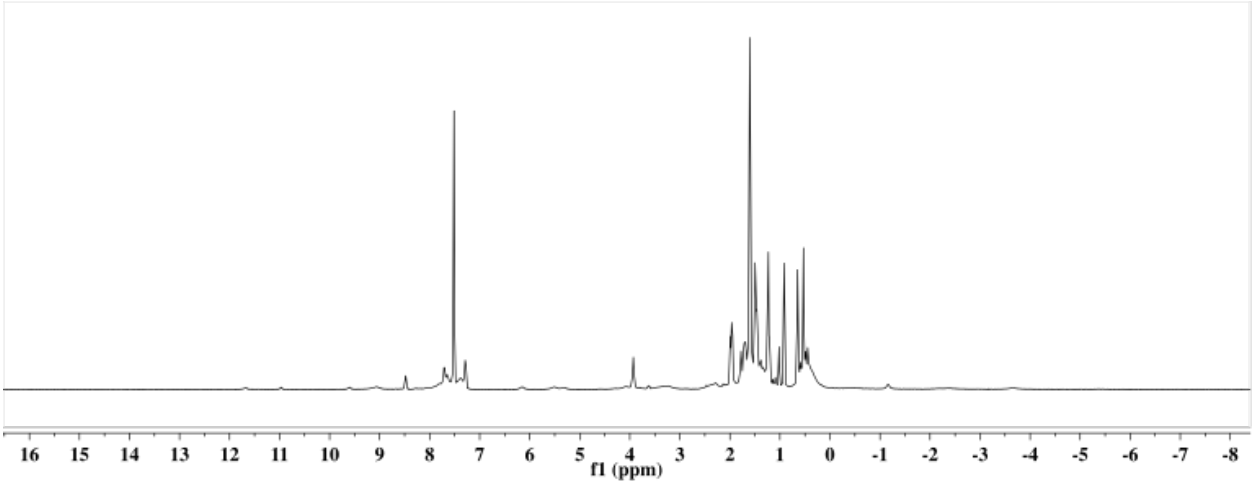

Figure S70. $^{31}P\{^{1}H\}$ spectrum of **10-CN^{t}Bu** after stirring under an H_2 atmosphere overnight. Starting material is observed with a minor amount of a decay product (likely $P_3^{B}(\mu\text{-}H)Fe(H)(CN^{t}Bu)_{13}$) and no identifiable **9**.

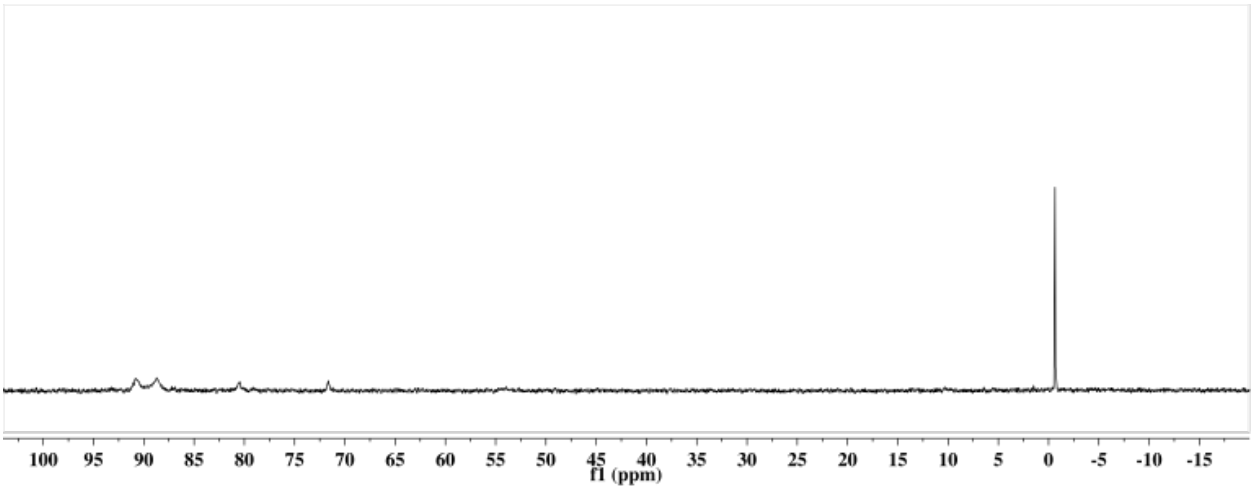

(13) H. Fong, M.-E. Moret, and J. C. Peters, *Organometallics,* 2013, **32**, 3053.

Figure S71. ^{1}H NMR (C_6D_6; 400 MHz) spectrum of **10-CN^{t}Bu** after stirring under an H_2 atmosphere overnight. Starting material is observed along with products of decay including new paramagnetic specie(s) and P_3^B(μ-H)Fe(H)(CN^{t}Bu).

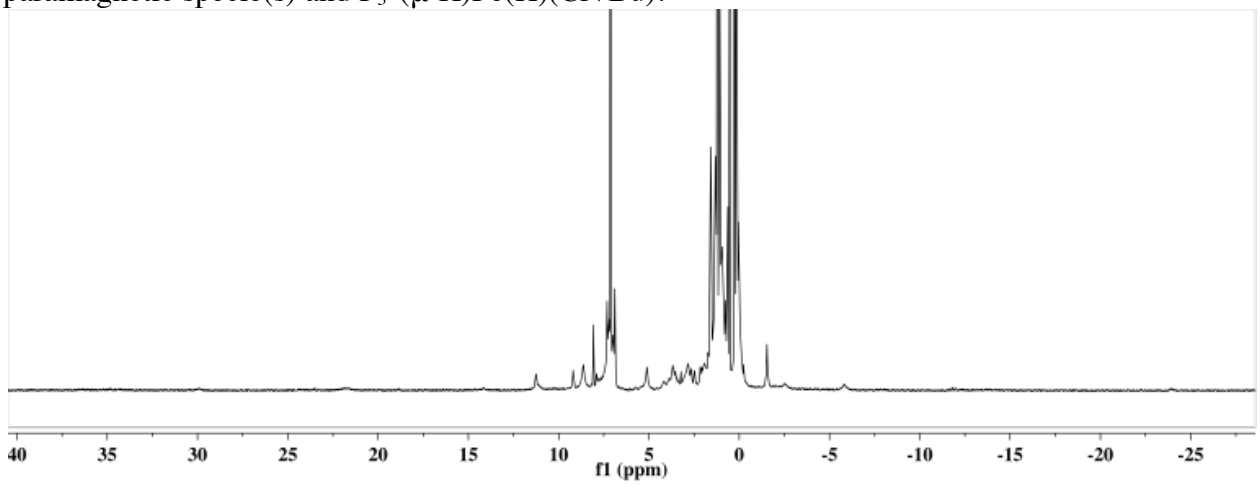

Transformation of **7** to **9** under a D_2 Atmosphere: Complex **7** (0.064 mmol) was prepared in solution at -78 °C under an N_2 atmosphere as above. This solution was transferred to a Schlenk tube with CN^{t}Bu (0.320 mmol, 5 equiv) added. The solution was frozen, the headspace was removed and backfilled with an atmosphere of D_2 and the mixture was thawed and allowed to warm to room temperature. The mixture was degassed by three freeze-pump-thaw cycles and the resulting solution was worked up according to the standard protocol (above). Examination of the product **9** showed no incorporation of deuterium with no observable intensity for the N-D or B-D-Fe stretches by IR spectroscopy.

Figure S72. IR spectra comparing authentic samples of unlabeled **9** (top), labeled **9-D$_2$** (middle), and the product mixture generated from unlabeled **7** under a D_2 atmosphere (bottom). Blue arrows highlight the positions of the N-H and B-H-Fe stretches and red arrows highlight the positions of the N-D and B-D-Fe stretches, which are absent in the spectrum of the reaction mixture.

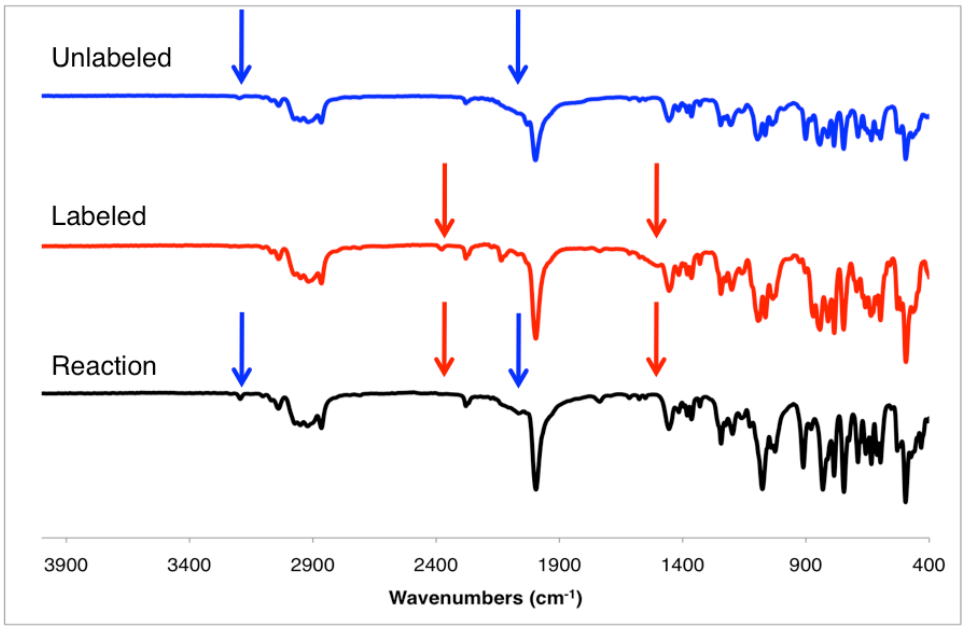

Alternative approaches to the release of N-fixed products:
In all cases, the disilylhydrazido(1-) complex **9** was prepared according to the procedure above. Quantification of liberated N-fixed products was done using the protocol described above for colorimetric detection of hydrazine and ammonia. Because the Fe-containing products of these reactions are ill-defined, some of the N-fixed products of these reactions may be derived from the HCl protonolysis step.

Thermolysis: Isolated **9** was dissolved in benzene and heated at 60 °C in a sealed Schlenk tube overnight, which resulted in complete consumption of the starting material. Fe containing products from these reactions could not be identified. (Run 1: NH_3 21%, N_2H_4 18%; Run 2: NH_3 23%; N_2H_4 20%)

Figure S73. Representative ^1H NMR spectrum generated from these reaction mixtures.

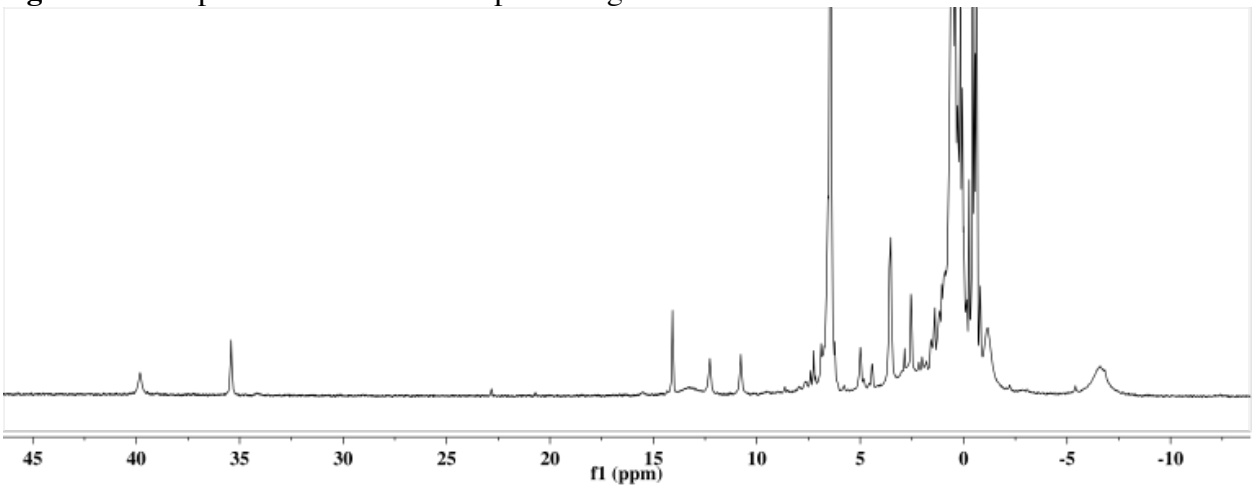

Figure S74. Corresponding $^{31}P\{^1H\}$ spectrum with resonances consistent with the presence of free phosphine species

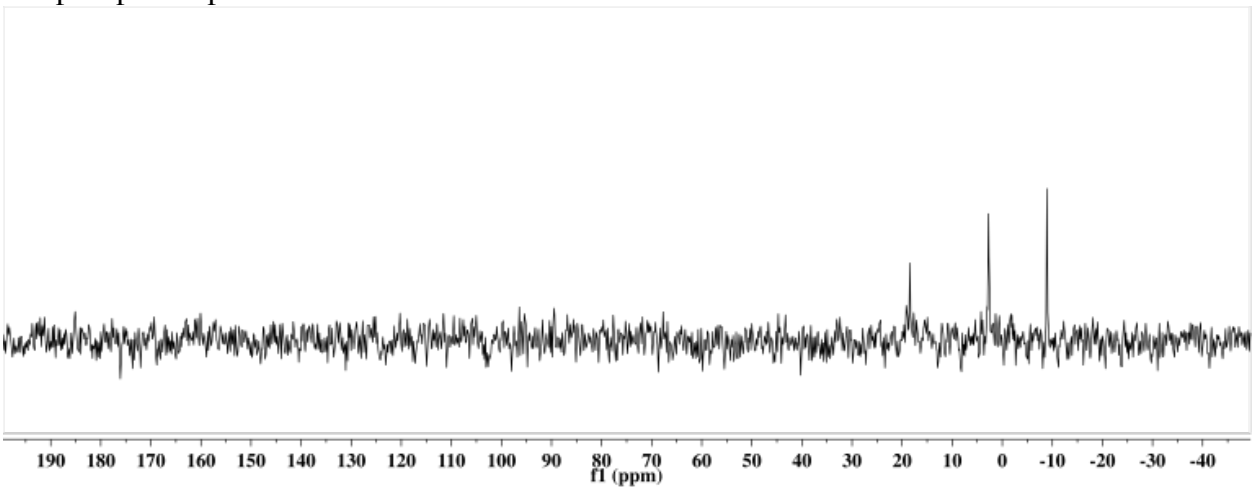

Thermolysis with additives: These reactions were analogous to the thermolysis reactions above, but with additional reagents added to the reaction mixtures. These additives did not appear to substantially perturb the product mixtures that were obtained.

Under an H_2 atmosphere: NH_3 12%, N_2H_4 28%

$PhSiH_3$ (5 equiv) added: NH_3 19%, N_2H_4 26%

Direct reaction of **8** with acid: We also explored the reactivity of **8** as generated *in situ*, towards exogenous acid. For the second run, crude **8** was isolated after stirring at room temperature by removing the solvent and extraction into pentane prior to treatment with acid. (Run 1: NH_3 8%, N_2H_4 42.5%; Run 2: 3.3%, N_2H_4: 47.6%).

Photolysis of **9**: Irradiation of a benzene solution of **9** with a Hg lamp at room temperature, resulted in the generation of species that were observed as the terminal product(s) of the thermal decay of **8**, consistent with the photodissociation of the CN^{t}Bu ligand.

Figure S75. Terminal product mixture observed by ^{1}H NMR upon thermal decay of complex **8**.

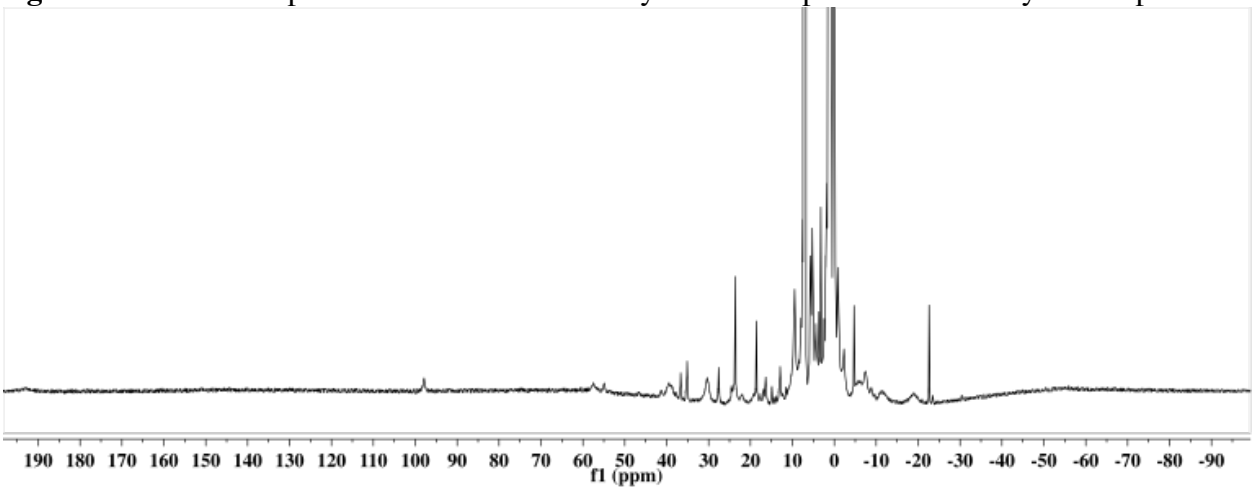

Figure S76. Product mixture observed by ^{1}H NMR upon Hg lamp irradiation of complex **9**.

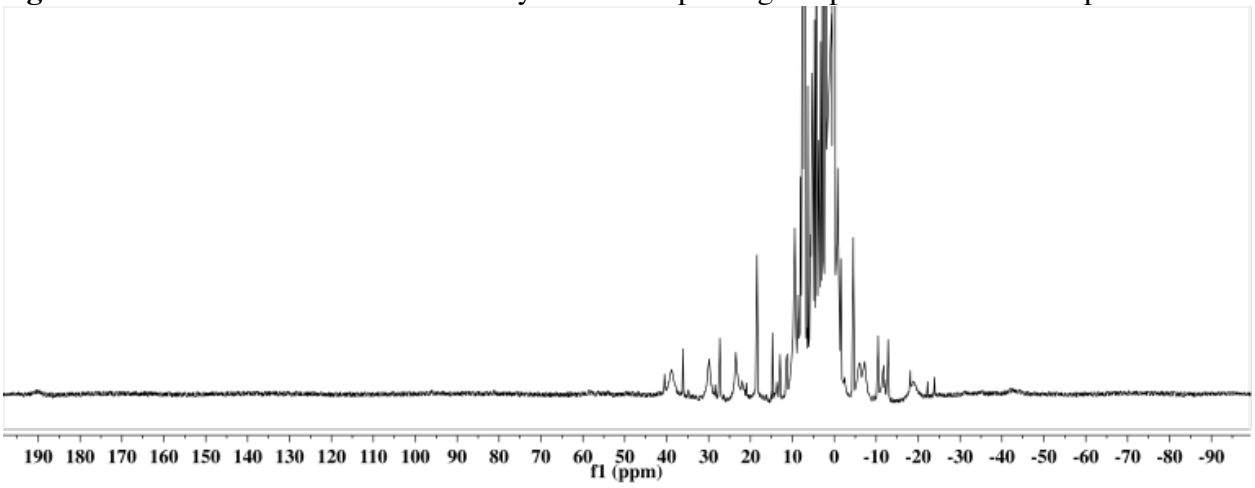

9. Crystallographic Details

Table S3. Crystallographic Details

	Dianion 2	Monoanion 4	Diazenido 5	Hydrazido(1-) 9	CN^{t}Bu H cation
Crystal system	Monoclinic	Monoclinic	Triclinic	Orthorhombic	Monoclinic
Crystal size (mm)	0.05 x 0.21 x 0.22	0.18 x 0.20 x 0.28	0.11 x 0.20 x 0.27	0.11 x 0.20 x 0.28	0.04 x 0.25 x 0.26
Formula	$C_{48}H_{86}BFeK_2N_2O_6P_3$	$C_{64}H_{95}BFeKN_2O_{10}P_3$	$C_{49}H_{85}BFeKN_2OP_3Si$	$C_{47}H_{81}BFeN_3P_3Si_2$	$C_{79}H_{91}B_2F_{24}FeNP_3$
Formula weight (g/mol)	1024.95	1251.08	944.99	903.90	1680.95
Space group	P n	P 21/c	P -1	P b c a	P 21/c
a (Å)	12.8973(7)	11.3464(4)	12.4653(18)	11.3085(5)	27.577(3)
b (Å)	12.5342(6)	35.5398(14)	13.091(3)	24.2407(12)	15.5573(16)
c (Å)	17.2106(8)	15.8541(6)	21.997(3)	37.5101(18)	38.526(4)
α (deg)	90	90	97.411(10)	90	90
β (deg)	98.668(2)	90.839(1)	95.734(4)	90	100.8630(10)
γ (deg)	90	90	117.826(8)	90	90
Z	2	4	2	8	8
V (Å^3)	2750.4(2)	6392.5(4)	3095.1(10)	10282.5(8)	16232(3)
Indep. Reflections	14778	24375	25264	17889	34202
R(int)	3.84	8.08	5.22	7.14	7.15
R1	3.15	3.89	3.97	5.67	7.48
wR2	6.90	8.72	10.14	12.58	19.84
GOF	1.02	1.04	1.03	1.19	1.12

Remarks on Crystal Structures:

[P_3^B(μ-H)Fe(H)(N_2)][K_2(THF)$_n$] 2. This compound crystallizes with two coordinated K countercations stabilized by interactions with the Fe-coordinated N_2 ligand, three total DME solvent molecules, and with an arene ring of the supporting ligand. One of the six phosphine ^{i}Pr groups was modeled as disordered over two positions (59:41). Refinement of this disorder was aided by the application of SIMU and RIGU restraints.

[P_3^BFe(H)(N_2)][K(benzo-15-crown-5)$_2$] 4. This compound crystallizes as a monomeric species with a crown encapsulated counter-cation in the absence of solvent. Two of the six total phosphine ^{i}Pr groups were modeled in a related disorder over two positions (64:36). Additionally, one of the K-coordinated crown moieties was modeled as rotationally disordered over two positions (56:44). Application of RIGU restraints aided in the refinement of these disorders.

[P_3^B(μ-H)Fe(H)(NNSi^{i}Pr$_3$)][K(THF)] 5. This complex crystallizes with one K-coordinated THF molecule and additional disordered solvent molecules in the asymmetric unit. The residual electron density associated with the disordered solvent was treated using SQUEEZE. The THF molecule was modeled as disordered over two positions (59:41) and this refinement was aided by RIGU restraints. One of the Si ^{i}Pr groups was modeled as disordered over two positions (77:23).

P_3^B(μ-H)Fe(NHN(Si(Me$_2$)CH$_2$CH$_2$SiMe$_2$))(CN^{t}Bu) 9. This compound crystallizes in the absence of solvent.

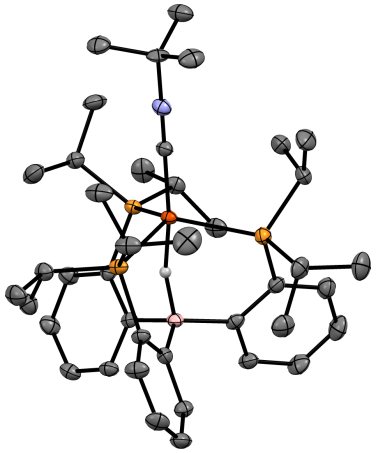

FigureS77. Representative structure of $[P_3^B(\mu\text{-H})Fe(CN^tBu)][B(C_8H_3F_6)_4]$ with displacement ellipsoids shown at 50% probability, with an additional, similar structure found in the asymmetric unit. C-bound H-atoms, solvent molecules and $B(C_8H_3F_6)_4$ counterions are omitted for clarity.

$[P_3^B(\mu\text{-H})Fe(CN^tBu)][B(C_8H_3F_6)_4]$. This compound crystallizes with two molecules in the asymmetric unit and two fully occupied cocrystallized pentane molecules and a third partially occupied pentane moiety (49%). The core iron structures had no disorder, but 7 of the 16 CF_3 groups were modeled as disordered over two positions (BAr_4^F 2: 79:21, 91:9, 73:26, 76:24; BAr_4^F 1: 75:25, 76:24, 54:46) and one of the pentane molecules was modeled as disordered over two positions (55:45). Refinement of these disorders was aided by the application of SIMU and RIGU restraints.

10. Bond Distances and Angles

Table S4. $[P_3^B(\mu\text{-H})Fe(H)(N_2)][K_2(THF)_n]$ 2.

Bond Distances (Å)		Bond Angles (degrees)	
Fe1-P1 (coord.)	2.1470(6)	P1-Fe1-P2	122.55(2)
Fe1-P2 (coord.)	2.1505(6)	Fe1-N1-N2	178.4(2)
Fe1-P3 (free)	4.5536(7)	B1-Fe1-N1	111.80(8)
Average Fe-P (coord.)	2.15	P1-Fe1-N1	124.03(7)
Fe1-N1	1.743(2)	P2-Fe1-N1	113.31(7)
Fe1-B1	2.749(3)		
Fe1-H1A-B1	1.69(3)		
Fe1-H	1.37(4)		
N1-N2	1.169(3)		

Table S5. $[P_3^BFe(H)(N_2)][K(benzo\text{-}15\text{-}crown\text{-}5)_2]$ 4.

Bond Distances (Å)		Bond Angles (degrees)	
Fe1-P1	2.1786(4)	P1-Fe1-P2	106.44(2)
Fe1-P2	2.2225(4)	P2-Fe1-P3	104.55(2)
Fe1-P3	2.2151(5)	P1-Fe1-P3	139.95(3)
Average Fe-P	2.21	Fe1-N1-N2	177.0(1)
Fe1-N1	1.800(1)	B1-Fe1-N1	177.79(5)
Fe1-B1	2.289(1)	P1-Fe1-N1	97.84(4)
Fe1-H	1.46(2)	P2-Fe1-N1	100.80(4)
N1-N2	1.132(2)	P3-Fe1-N1	100.63(4)

Table S6. $[P_3^B(\mu\text{-H})Fe(H)(NNSi^iPr_3)][K(THF)]$ 5.

Bond Distances (Å)		Bond Angles (degrees)	
Fe1-P1 (coord.)	2.2202(7)	P1-Fe1-P2	116.59(2)
Fe1-P2 (coord.)	2.21758(7)	Fe1-N1-N2	169.31(9)
Fe1-P3 (free)	4.4191(8)	B1-Fe1-N1	119.31(4)
Average Fe-P (coord.)	2.22	P1-Fe1-N1	125.04(4)
Fe1-N1	1.672(1)	P2-Fe1-N1	117.58(4)
Fe1-B1	2.791(1)	N1-N2-Si1	132.31(9)
Fe1-H1A-B1	1.8245		
Fe1-H	1.45(1)		
N1-N2	1.249(2)		

Table S7. $P_3^B(\mu\text{-H})Fe(NHN(Si_2))(CN^tBu)$ 9.

Bond Distances (Å)		Bond Angles (degrees)	
Fe1-P1 (coord.)	2.227(1)	P1-Fe1-P2	112.84(3)
Fe1-P2 (coord.)	2.2338(7)	Fe1-N1-N2	145.8(1)
Fe1-P3 (free)	5.5746(8)	B1-Fe1-N1	92.39(7)
Average Fe-P (coord.)	2.23	P1-Fe1-N1	125.91(6)
Fe1-N1	1.824(2)	P2-Fe1-N1	115.86(6)
Fe1-B1	2.885(2)	P1-Fe1-C1	89.41(6)
Fe1-H1A-B1	1.9049	P2-Fe1-C1	97.38(6)
N1-H1	0.92(3)	C1-Fe1-N1	106.00(8)
N1-N2	1.404(2)	B1-Fe1-C1	161.47(7)
Fe1-C1	1.811(2)		

Table S8. $[P_3^B(\mu\text{-H})Fe(CN^tBu)][B(C_8H_3F_6)_4]$.

Bond Distances (Å)		Bond Angles (degrees)	
Fe1-P1	2.390(1)	P1-Fe1-P2	117.24(5)
Fe1-P2	2.406(1)	P2-Fe1-P3	113.68(5)
Fe1-P3	2.392(1)	P1-Fe1-P3	115.03(5)
Fe2-P4	2.406(1)	P4-Fe2-P5	114.14(5)
Fe2-P5	2.398(1)	P5-Fe2-P6	113.84(5)
Fe2-P6	2.378(1)	P4-Fe2-P6	118.24(5)
Average Fe-P	2.395	P1-Fe1-C1	101.5(1)
Fe1-C1	1.869(4)	P2-Fe1-C1	102.2(1)
Fe2-C42	1.869(4)	P3-Fe1-C1	104.4(1)
Fe1-B1	2.763(5)	P4-Fe2-C42	103.8(1)
Fe2-B2	2.769(5)	P5-Fe2-C42	103.1(1)
Fe1-H1-B1	1.39(6)	P6-Fe2-C42	100.8(1)
Fe2-H2-B2	1.49(5)		